AEROELASTIC FLUTTER VIBRATION ENERGY HARVESTING: MODELING, TESTING, AND SYSTEM DESIGN

A Dissertation

Presented to the Faculty of the Graduate School

of Cornell University

In Partial Fulfillment of the Requirements for the Degree of

Doctor of Philosophy

by

Matthew Bryant

May 2012

AEROELASTIC FLUTTER VIBRATION ENERGY HARVESTING: MODELING, TESTING, AND SYSTEM DESIGN

Matthew Bryant, Ph. D.

Cornell University 2012

The rapid proliferation of wireless sensors and microelectronics has spurred considerable interest in developing small scale devices that convert ambient energy sources to electrical power. Such "energy harvesting" devices could thus eliminate the need for hardwired power and extend the useful lifespan of a wireless sensor beyond the finite capacity of a battery. Piezoelectric materials, which directly convert mechanical strain to electrical energy, have been extensively investigated in recent years as a potential means to harvest energy from mechanical vibrations. This research has predominately focused on harvesting energy from preexisting vibrating host structures through base excitation of cantilevered piezoelectric beams. This approach, while simple to implement, inherently restricts the application of piezoelectric energy harvesting technology to environments where suitable vibrations are available.

This dissertations proposes and investigates a novel piezoelectric energy harvesting device that simultaneously generates vibrations and harvests energy from an ambient fluid flow by inducing an aeroelastic flutter instability in a simple structure. The proposed device is studied through a combination of analytic modeling and wind tunnel experimentation. A model of this device that captures the three-way coupling between the structural, unsteady aerodynamic, and electrical aspects of the system is developed. The model is applied to predict the flow speed required for energy harvesting using linear stability analysis, and is generalized to account for aerodynamic nonlinearities that lead to flutter limit cycle behavior over a broad range of flow

speeds. Wind tunnel test results are presented to determine empirical aerodynamic model coefficients and to characterize the power output and flutter frequency of the harvester as functions of incident wind speed. The model is then used to investigate the key design parameters of the system and determine the sensitivity and effective range of each parameter in affecting the characteristics of the aeroelastic instability driving the energy harvester. Finally, wind tunnel testing and flow visualization investigate the aerodynamic interactions between multiple flutter energy harvesters operating simultaneously. These experiments reveal synergistic wake-structure interactions than can be used to enhance the array performance, allowing the harvesters to produce more power when operating in close proximity than in a steady free stream flow.

BIOGRAPHICAL SKETCH

Matthew Bryant earned a Bachelor's of Science degree in Mechanical Engineering from Bucknell University in 2007. While an undergraduate, Matthew participated in the Bucknell Institute for Leadership in Technology and Management fellowship program, and interned at General Electric Rail in Erie, PA. During his undergraduate studies, Matthew also worked as a Peer Tutor in physics and calculus, and as a lab teaching assistant and grader for Fluid Mechanics, Mechanical Design, and Thermodynamics courses. Matthew was a member of the Bucknell Baja SAE Team, which designs and builds an amphibious all-terrain vehicle for an annual collegiate competition. During his senior year, Matthew designed and built an experimental hydraulic four-wheel steering system for the Baja car and drove the car in the four-hour endurance race at the Baja UCF 2007 competition. Matthew graduated first in his class in both the Mechanical Engineering major and the College of Engineering. He received the Oliver J Decker Prize and the Ernest and Josephine Christensen Award for Outstanding Engineering Graduate.

In 2007, Matthew began graduate studies at Cornell University, where he joined the Laboratory for Intelligent Machine Systems under the direction of Dr. Ephrahim Garcia as a Graduate Research Assistant. During his graduate studies, Matthew worked as Head Teaching Assistant for Mechatronics three semesters and, in 2009, received a Research Opportunity Program Appointment from the U.S. Department of Homeland Security. In 2009 Matthew was married to Kirsten Elzer, who was also working toward her Ph.D. at Cornell University in the field of Molecular Medicine. In 2011 he was awarded his Master's of Science degree in Mechanical Engineering for his work on aeroelastic flutter vibration energy harvesting. Matthew

continued his research on flutter energy harvesting at Cornell University in pursuit of his doctorate. Matthew has published one journal paper in the ASME Journal of Vibrations and Acoustics, one paper in Smart Materials and Structures Journal, and a third paper has been accepted for publication in the Journal of Intelligent Material Systems and Structures.

For Kirsten, my wife and inspiration.

ACKNOWLEDGEMENTS

I am forever grateful to my loving wife Kirsten, whose seemingly infinite patience, support, and motivation helped me through many challenging times throughout my studies. I would like to thank my parents, James and Carolyn, who always encouraged me to pursue my goals and education to the fullest. I thank my advisor, Prof. Ephrahim Garcia for his guidance, inspiration, and advice in my academic endeavors. I also acknowledge my lab mates, Allen Hurst, Michael Shafer, Mitch Walters, and John Dietl for helping me to maintain perspective through many long hours of Matlab and the wind tunnel. I thank Ranjeev Mahtani, Eric Wolff, Michael Isenberg, Jaebin Choi, and Alex Schlichting for their assistance in fabricating experimental hardware and collecting wind tunnel data for my research. I also gratefully acknowledge funding support for my research and graduate studies from the National Science Foundation, the U.S. Department of Homeland Security, the Cornell Center for a Sustainable Future, and the Cornell University McManus Research Award.

TABLE OF CONTENTS

CHAPTER 3

WAKE SYNERGIES ENHANCE PERFORMANCE IN AEROELASTIC VIBRATION ENERGY HARVESTING

LIST OF FIGURES

CHAPTER 1

CHAPTER 2

CHAPTER 3

LIST OF TABLES

CHAPTER 1

CHAPTER 2

CHAPTER 3

LIST OF SYMBOLS

CHAPTER 1

a	=	dimensionless flap joint axis location
b	=	flap semichord
C	=	viscous damping coefficient
C_D, C_L, C_M	=	drag, lift, and moment coefficients respectively
C_z	=	general aerodynamic coefficient
C_P	=	piezoelectric capacitance
c^E	=	constant electric field PZT stiffness
c_M, c_S	=	epoxy matrix and beam substructure stiffness respectively
$D(t)$	=	drag force
d_{31}	=	piezoelectric constant
e	=	dimensionless flap center of mass location
$f(x,t)$	=	beam aerodynamic load function
$h(t)$	=	flap heave deflection coordinate
I_C, I_P	=	flap mass moment of inertia about center of mass and joint axis respectively
K	=	stiffness matrix
$L(t)$	=	lift force
ℓ, ℓ_M, ℓ_P	=	length of bender, epoxy layer, and piezo respectively
m_F, m_T	=	flap mass and total bender tip mass respectively
M	=	number of aerodynamic modes
$M_{1/4}(t)$	=	quarter chord pitching moment

$M_{M,}$, M_P, M_S	=	mass matrix for epoxy, piezo, and substrate respectively
N	=	number of structural modes
Q	=	generalized force
q	=	charge
R	=	resistive load
$\underline{r}(t)$	=	bender deflection temporal coordinate
S	=	strain
s	=	flap span
T	=	kinetic energy
t	=	time
t_M, t_P, t_S	=	thickness of epoxy, piezo, and substrate respectively
U	=	free stream wind speed
$u(x,t)$	=	beam deflection coordinate
V	=	potential energy
v	=	instantaneous incident wind speed
$V_{M,}$, V_P, V_S	=	volume of epoxy, piezo, and substrate layers respectively
w	=	width
x	=	position along bender length
x_θ	=	flap static unbalance parameter
α	=	effective angle of attack
$\overline{\delta W}$	=	virtual work
ε^S	=	constant strain permittivity
$\underline{\phi}(x)$	=	mode shape

λ = induced flow state

θ = angular position

ρ_M, ρ_P, ρ_S = density of epoxy, piezo, and substrate materials respectively

ρ_∞ = free stream air density

τ = dimensionless time

ω = angular frequency

subscripts

T = tip mass

B = bender

F = flap

h = heave

θ = rotational

CHAPTER 2

a = dimensionless flap joint axis location

b = flap semichord

C = viscous damping coefficient

C_P = piezoelectric capacitance

c^E = constant electric field PZT stiffness

c_M, c_S = epoxy matrix and beam substructure stiffness respectively

$D(t)$ = drag force

d_{31} = piezoelectric constant

e = dimensionless flap center of mass location

$f(x,t)$	=	beam aerodynamic load function
$h(t)$	=	flap heave deflection coordinate
I_P	=	flap mass moment of inertia about hinge joint axis
I_P^*	=	dimensionless flap moment of inertia about hinge joint axis
$K_{M,}$, K_P, K_S	=	stiffness matrix for epoxy, piezo, and substrate respectively
K_θ	=	stiffness of hinge joint
$L(t)$	=	lift force
ℓ, ℓ_M, ℓ_P	=	length of bender, epoxy layer, and piezo respectively
m_F, m_{NR}	=	flap mass and non-rotating bender tip mass respectively
$M_{1/4}(t)$	=	quarter chord pitching moment
$M_{M,}$, M_P, M_S	=	mass matrix for epoxy, piezo, and substrate respectively
N	=	number of structural modes
q	=	charge
R	=	resistive load
$\underline{r}(t)$	=	bender deflection temporal coordinate
s	=	flap span
t	=	time
t_M, t_P, t_S	=	thickness of epoxy, piezo, and substrate respectively
$u(x,t)$	=	beam deflection coordinate
w	=	width
x	=	position along bender length
x_θ	=	flap static unbalance parameter

ε^S = constant strain permittivity

$\phi(x)$ = mode shape

θ = angular position

ρ_M, ρ_P, ρ_S = density of epoxy, piezo, and substrate materials respectively

ρ_∞ = free stream air density

ω = angular frequency

ω_θ = zero wind speed flap rotation natural frequency

CHAPTER 3

f = flutter vibration frequency

$t_{0,i}$, $t_{1,i}$ = starting and ending times of the i^{th} half cycle of oscillation

C_P = piezoelectric capacitance

L = overall length of a single energy harvester

C = number of half oscillation cycles in a full data set

N = total number of energy harvesters in the array

$P_{avg,i}$ = average power for the i^{th} half cycle of oscillation

P_{AVG} = average power for a full data set

$\overline{P}_{AVG}$ = normalized average power for a full data set

R_{opt} = optimal resistive load

U_∞ = free stream flow velocity

V = voltage history through the load resistor

$V_{rms,i}$ = root-mean squared voltage for the i^{th} half cycle of oscillation

X	=	stream-wise separation distance
Y	=	cross-stream separation distance
η_{ARRAY}	=	aerodynamic array efficiency
σ	=	standard deviation of output power
φ	=	phase difference between energy harvester output voltages
ω	=	flutter vibration angular frequency

CHAPTER 1
MODELING AND TESTING OF A NOVEL AEROELASTIC FLUTTER ENERGY HARVESTER

1. Abstract

This chapter proposes a novel piezoelectric energy harvesting device driven by aeroelastic flutter vibrations of a simple pin connected flap and beam. The system is subject to a modal convergence flutter response above a critical wind speed and then oscillates in a limit cycle at higher wind speeds. A linearized analytical model of the device is derived to include the effects of the three-way coupling between the structural, unsteady aerodynamic, and electrical aspects of the system. A stability analysis of this model is presented to determine the frequency and wind speed at the onset of the flutter instability, which dictates the cut-in conditions for energy harvesting. In order to estimate the electrical output of the energy harvester, the amplitude and frequency of the flutter limit cycle is also investigated. The limit cycle behavior is simulated in the time domain with a semi-empirical nonlinear model that accounts for the effects of the dynamic stall over the flap at large deflections. Wind tunnel test results are presented to determine empirical aerodynamic model coefficients and to characterize the power output and flutter frequency of the energy harvester as functions of incident wind speed.

2. Introduction

Several recent studies have explored the possibility of using piezoelectric materials to harvest energy from flowing fluids using a variety of mechanisms. While traditional piezoelectric energy harvesting research has predominantly focused on extracting energy from

preexisting vibrating host structures (Anton and Sodano, 2007), the fluid energy harvesting problem must address not only the transduction of vibration to electrical energy, but the generation of vibrations from the fluid flow as well. Thus the fluid flow energy harvesting problem introduces a three-way coupling of structural, electrical, and fluid dynamics, all of which must be considered in system modeling and design. A number of groups have investigated piezoelectric "eels" or "flags" that are induced to undergo oscillating bending stresses due to the effects of vortices shed from an upstream bluff body. The bluff body periodically sheds vortices from either side, producing oscillating surface pressures acting on the flexible downstream piezoelectric element and causing it to flap or wave in the flow. This concept has been proposed for use in air (Robins et al., 2001) as well as in water (Allen and Smits, 2001, Taylor et al., 2001, Pobering and Schwesinger, 2004). A traditional rotary windmill design was adapted to explore piezoelectric energy harvesting by using a cam system to induce cyclic bending of a set of radially arranged piezoelectric bimorphs (Priya et al, 2005). The continuous rotation of the windmill shaft is converted to alternating motion of a series of stoppers that deflect the tips of the piezoelectric bimorphs. Piezoelectric damping and energy harvesting of vibrations of cantilevered pipes carrying flowing fluid have also been the subject of recent work (Elvin and Elvin, 2009).

Flow induced vibrations are typically regarded as undesirable and destructive phenomena that occur in a broad range of structures. Such effects occur in systems ranging from heat exchanger tube rows, to smokestacks, to aircraft components (Blevins, 2001). Aeroelastic flutter of aircraft wings and empennage structures is perhaps one of the most dramatic and familiar of these flow induced vibration effects. This type of flutter is distinct from other aeroelastic vibrations because of the mechanism responsible for the instability. While many other types of

flow induced vibration are the result of vortex shedding effects (Khalak and Williamson, 1999) wing flutter results from the convergence of two structural modes, giving it the moniker modal convergence flutter or coupled mode flutter (Dowell et al. 1980, Hodges and Pierce, 2002). The interaction of multiple degrees of freedom also distinguishes modal convergence flutter from galloping flutter, which is a single degree of freedom phenomenon that causes vibrations of bluff bodies (van Oudheusden, 1996). In modal convergence flutter, aerodynamic forces drive the natural frequencies of the two modes, generally a torsion mode and a bending mode, to converge near the critical flutter wind speed. Above the flutter wind speed, energy from the fluid flow is transferred to the structure, causing one of the system poles to become unstable and leading to growing flutter oscillations (Dowell et al. 1980, Hodges and Pierce, 2002). These oscillations grow in amplitude until the deflections become sufficient for system nonlinearities to create limit cycle behavior or for structural failure to occur. It has been noted in the literature that this type of flutter exhibits less sensitivity to structural damping forces than other mechanisms of flow induced vibrations (Blevins, 2001, Dowell et al., 1980). This characteristic makes modal convergence flutter an ideal candidate to be used in energy harvesting; the piezoelectric energy extraction and charging dynamics of any attached energy storage elements will have a relatively small effect on the flutter vibrations. We propose a novel piezoelectric energy harvesting mechanism driven by modal convergence flutter vibrations of a simple cantilevered piezoelectric beam and a pin connected flap.

3. Experimental Setup

The aeroelastic energy harvesting apparatus, as shown in Fig. 1.1, consists of a rigid flap connected by a ball bearing revolute joint to the tip of a flexible 301 stainless steel beam. A pair

of MIDE Quickpack QP10N piezoelectric patches are laminated to the beam at the root end to provide electromechanical transduction, as illustrated by Figure 1.2. The beam root is cantilevered to a streamlined sting for mounting in the wind tunnel. This design creates an aeroelastic system with two coupled degrees of freedom, bending deflection of the beam and rotation of the flap about the bearing joint. This system is thus subject to a modal convergence flutter response, which provides the driving mechanism for the energy harvester.

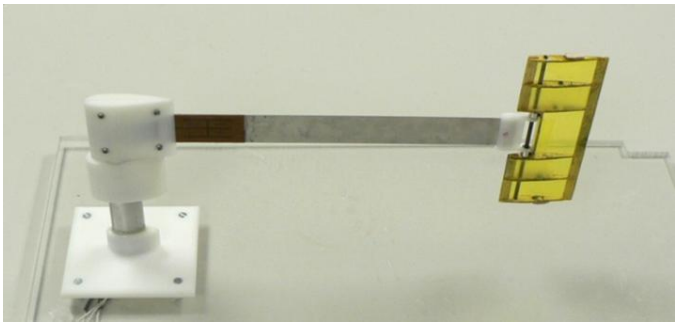

Figure 1.1 Photograph of the aeroelastic power harvester design.

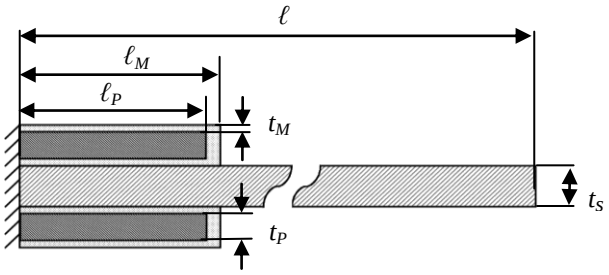

Figure 1.2 Schematic view of the bender and Quickpack piezoelectric patches with dimensions defined.

The physical, mechanical, and electromechanical properties of the device and materials used in the modeling of the system are summarized in Table 1.1 below. Table 1.2 gives the mass, inertia, and dimensional parameters for the flap, which was constructed with a NACA0012

airfoil profile. The NACA0012 profile was selected because published aerodynamic properties, such as those determined by Sheldahl and Klimas (1981), are widely available for this airfoil.

Table 1.1 Physical, mechanical, and electromechanical parameters of the aeroelastic energy harvester.

Parameter	*Symbol*	*Value*	*Units*
Physical:			
bender length	ℓ	25.4	cm
bender width	w	2.54	cm
beam substructure thickness	t_s	0.381	mm
PZT layer thickness	t_P	0.254	mm
PZT patch length	ℓ_P	4.60	cm
PZT patch width	w_P	2.06	cm
epoxy matrix layer thickness	t_M	0.0254	mm
epoxy matrix length	ℓ_M	4.84	cm
epoxy matrix width	w_M	2.5	cm
beam substructure density	ρ_S	7850	kg/m^3
PZT density	ρ_P	7700	kg/m^3
epoxy matrix density	ρ_m	2150	kg/m^3
Mechanical:			
beam substructure stiffness	c_S	212	GPa
PZT stiffness, open circuit	c^E	67	GPa
epoxy matrix stiffness	c_M	2.5	GPa
Electromechanical:			
piezoelectric constant	d_{31}	-190	pm/V
constant strain permittivity	ε^S	15.93	nF/m

Table 1.2 Physical parameters of the NACA0012 profile flap.

Parameter	*Symbol*	*Value*	*Units*
flap and support mass	m_T	9.66	g
flap mass	m_F	6.50	g
flap mass moment of inertia	I_P	17.2	g cm^2
flap span	s	13.6	cm
flap semichord	b	2.97	cm
flap static unbalance	x_θ	0.237	

Wind tunnel testing is conducted in a low speed, open-circuit wind tunnel with a 25×25×100 cm test section with a maximum wind speed of about 9.1 m/s. The free stream air speed during wind tunnel testing is measured with an Omega HHF42 probe hot wire anemometer and the output of the piezoelectric patches are plotted using an Agilent DSO6014A digital oscilloscope.

4. System Modeling

The aeroelastic energy harvester can be represented by adapting the wing section model often used in aeroelasticity literature (Hodges and Pierce, 2002). This method is used to perform flutter analyses on aircraft wing and empennage structures by examining a typical airfoil section of the structure. The stiffness of the structure is represented by hypothetical compression-extension and torsion springs placed at the elastic axis. In order to adapt this representation to the present study, the linear spring must be replaced with an appropriate beam model of the piezoelectric bender, and the torsion spring is eliminated because the revolute joint is assumed to have no stiffness. The typical section for the aeroelastic energy harvester flap is a uniform thin airfoil as shown in Figure 1.3. A uniform lift distribution across the span of the flap is assumed.

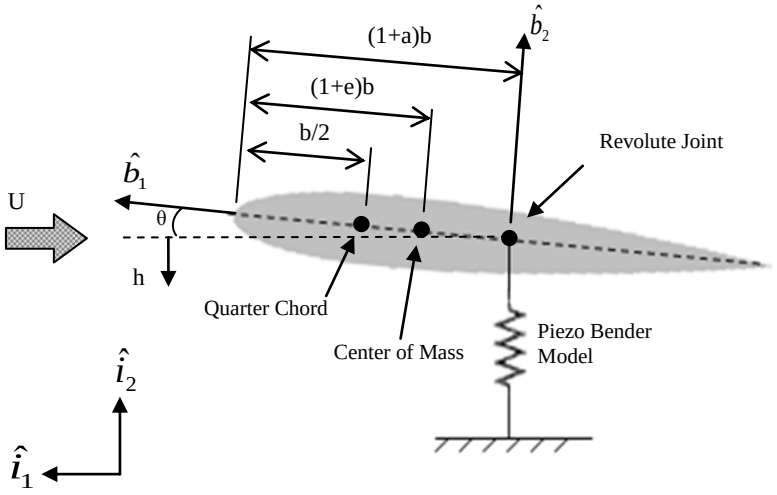

Figure 1.3 Section representation of the aeroelastic energy harvester describing the airfoil physical parameters.

5. Flutter Boundary Analysis

The flutter boundary, or set of flow conditions at which flutter emerges, is a critical design parameter to the aeroelastic energy harvester. For a given air density, the wind speed at the flutter boundary will determine the minimum wind speed required for the energy harvester to operate. This value, often referred to as the "cut-in wind speed" in wind power parlance, can be determined analytically by combining aircraft flutter analysis models with elasto-dynamic, piezoelectric coupling models to form the aeroelastic energy harvester system. In particular, we have fused the linear aeroelastic wing section model of Hodges and Pierce (2002), the Euler-Bernoulli piezoelectric bender model of Sodano et al. (2004), and the unsteady aerodynamic model of Peters et al. (1995) to create a coupled aeroelastic-electromechanical system model.

5.1 Linear System Model

Hamilton's principle was employed to combine both the aeroelastic and electromechanical system models. Following the energy formulation, the total system kinetic and potential energies, including the contributions from the flap assembly, beam, and piezoelectric patches must be defined. The system kinetic and potential energies, respectively, can be expressed by

$$T = \frac{1}{2}\left[m_T \dot{h}^2 + 2 m_F b x_\theta \dot{h}\dot{\theta} + I_p \dot{\theta}^2 + \int_{V_S} \rho_S \dot{\underline{u}}^T \dot{\underline{u}} dV_S + \int_{V_M} \rho_M \dot{\underline{u}}^T \dot{\underline{u}} dV_M + \int_{V_P} \rho_P \dot{\underline{u}}^T \dot{\underline{u}} dV_P \right] \quad (1)$$

$$V = \frac{1}{2}\left[\int_{V_S} \underline{S}^T c_S \underline{S} dV_S + \int_{V_M} \underline{S}^T c_M \underline{S} dV_M + \int_{V_P} \underline{S}^T c^E \underline{S} dV_P - \int_{V_P} \underline{S}^T e_P{}^T \underline{E} dV_P - \int_{V_P} \underline{E}^T e_P \underline{S} dV_P - \int_{V_P} \underline{E}^T \varepsilon^S \underline{E} dV_P \right] \quad (2)$$

where h and θ are the flap heave and pitch deflection coordinates, respectively, as depicted in Figure 1.3, m_F is the mass of the flap, m_T is the total mass attached to the beam tip, and I_p is the mass moment of inertia of the flap about the pin joint. The terms ρ_S, ρ_m, and ρ_P are the beam substrate, epoxy matrix, and piezo densities, respectively, and the variables V_S, V_m, and V_P are the beam substrate, epoxy matrix, and piezo volumes, respectively. The bender displacement is the transverse direction is u, and S and E represent the beam strain and electric field, respectively. The term c_S is the substrate elastic modulus, c^E is the piezo elastic modulus at short circuit, e_P is the piezo coupling coefficient, ε^S is the piezo dielectric or permittivity constant at constant strain (Sodano et al., 2004). Finally, x_θ, is the flap static unbalance parameter, which can be related to the parameters shown in Figure 1.3 by

$$x_\theta = e - a \quad (3)$$

The beam deflection *u(x,t)* can be expressed in terms of assumed beam mode shapes and a temporal coordinate using the Rayleigh-Ritz modal summation method as

$$u(x,t) = \sum_{i=1}^{N} \phi_i(x) r_i(t) = \underline{\phi}(x)\underline{r}(t) \tag{4}$$

where $\phi_i(x)$ is the beam mode shape, $r_i(t)$ is the temporal coordinate, and *N* is the number of mode shapes to be considered. The flap heave displacement, *h(t)*, can also be expressed in this coordinate framework as

$$h(t) = u(\ell,t) = \underline{\phi}(\ell)\underline{r}(t) \tag{5}$$

where ℓ is the length of the bender. The generalized forces acting on the system in the heave and pitch directions can be expressed in terms of the aerodynamic forces as

$$Q_h = -\underline{\phi}(\ell)^T L(t) \tag{6}$$

$$Q_\theta = M_{\frac{1}{4}}(t) + b\left(\frac{1}{2} + a\right)L(t) \tag{7}$$

where *L(t)* is the total lift force and $M_{1/4}(t)$ is the total pitching moment about the ¼ chord of the airfoil. In addition to the aerodynamic forces acting on the flap, the beam itself also experiences aerodynamic loads. The elastic bender is subject to distributed aerodynamic loading as it deflects normal to the flow, effectively changing the bending stiffness and damping as a function of incident wind speed. The virtual work done by the distributed beam aerodynamic forces can be written as

$$\overline{\delta W}_{beam} = -\delta\underline{r}(t)\int_0^{\ell} f(x,t)\underline{\phi}(x)^T dx \tag{8}$$

where $f(x,t)$ is a function describing the beam aerodynamic loads. Therefore, the generalized force due to the beam aerodynamic loading is given by

$$Q_{h,beam} = \int_0^{\ell} f(x,t)\underline{\phi}(x)^T dx \tag{9}$$

Lagrange's equations can now be applied to the above relations with bender deflection $\underline{r}(t)$, flap pitch deflection $\theta(t)$, and charge $q(t)$ as the generalized coordinates. The outputs of the piezoelectric patches are assumed to be wired in parallel and connected across a resistive load, R, to facilitate convenient measurement of the output current and power. Viscous damping terms are also added to allow for approximation of the structural damping in the bender and dissipation in the pin joint. After grouping terms, the system model is given by

$$\begin{aligned}&\left(M_S + M_M + M_P + m_T \underline{\phi}(\ell)^T \underline{\phi}(\ell)\right)\ddot{\underline{r}} + m_F b x_\theta \underline{\phi}(\ell)^T \ddot{\theta} + C_h \dot{\underline{r}} + (K_S + K_M + K_P)\underline{r} - \Theta C_p^{-1} q \\ &= -\underline{\phi}(\ell)^{\mathrm{T}} \mathrm{L} + \int_0^{\ell} f \underline{\phi}^{\mathrm{T}} \mathrm{dx}\end{aligned} \tag{10}$$

$$m_F b x_\theta \underline{\phi}(\ell)\ddot{\underline{r}} + I_P \ddot{\theta} + C_\theta \dot{\theta} = M_{1/4} + b\left(\frac{1}{2} + a\right)L \tag{11}$$

$$R\dot{q} - C_P^{-1}\Theta \underline{r} + C_P^{-1} q = 0 \tag{12}$$

where the matrices M_S, M_M, M_P, K_S, K_M, and K_P are the resulting groups of integrals, C_P and Θ are the piezo capacitance and electromechanical coupling matrices respectively, and the terms C_h and C_θ are the viscous damping terms for the heave and pitch degrees of freedom, $L(t)$ is the lift force acting on the flap, and $M_{1/4}(t)$ is the pitching moment acting at the flap ¼ chord point.

5.2 Linear Aerodynamic Model

The aerodynamic lift force and pitching moment acting on the structure are modeled using the unsteady flow model of Peters et al. (1995). While traditional, steady flow

aerodynamic expressions would provide a simpler model, unsteady effects are generally important in aeroelastic vibrations. The pitching and heaving motions of the flap have significant effects on the air flow, prompting vortices to be shed from the trailing edge, which in turn affect the flow incident on the flap. In addition, because of the oscillatory motions of the structure, the direction of the wind vector relative to the structure is not fixed. Therefore, a more complex, unsteady aerodynamic model that accounts for both circulatory and non-circulatory terms in the flow must be adopted in the analysis of dynamic aeroelastic structures (Hodges and Pierce, 2002).

The unsteady aerodynamics models available in the literature can be broadly divided into two categories, those that assume simple harmonic motion of the structure and those that do not. The prior models, including that of Theodorsen (1934) offer a simpler approach but are only applicable at the flutter stability boundary condition, not in transient vibrations. The latter category adds additional complexity but allows analysis of the system behavior and eigenvalues below the critical flutter speed and in transients. Among the latter, we implement the finite state, induced flow theory of Peters et al. (1995) because it offers a time domain, state space representation that allows for convenient simulation of the system.

This model approximates the effects of the unsteady airloads for invicid, incompressible flows by using induced flow terms to account for the effects of shed vortices on the flow near the airfoil. The wind velocity near the foil is the free stream velocity plus an additional local induced flow component (Peters et al., 1995). The resulting expressions for the lift and moment acting on the flap can be summarized as follows:

$$L(t) = \pi\rho_\infty s b^2 \left(\ddot{h}(t) + U\dot{\theta}(t) - ba\ddot{\theta}(t)\right) + 2\pi\rho_\infty sUb\left[\dot{h}(t) + U\theta(t) + b\left(\frac{1}{2} - a\right)\dot{\theta}(t) - \lambda_0(t)\right] \quad (13)$$

$$M_{1/4}(t) = -\pi\rho_\infty s b^3\left[\frac{1}{2}\ddot{h}(t) + U\dot{\theta}(t) + b\left(\frac{1}{8} - \frac{a}{2}\right)\ddot{\theta}(t)\right] \tag{14}$$

where ρ_∞ is the air density, *s* is the span of the flap, and λ_0(t) is the induced flow velocity. The parameters *U, h(t),* and *θ(t)* are defined in Figure 1.3 and are the free stream wind velocity, the heave deflection of the flap, and the rotation angle of the flap respectively. The induced flow is then approximated by a series of induced flow states λ_n(t) given by:

$$\lambda_0(t) \approx \frac{1}{2}\sum_{n=1}^{M} b_n \lambda_n(t) \tag{15}$$

where *M* is the number of induced flow states to be included in the analysis and b_n are a series of least squares coefficients. The model states that a system of *M* differential equations govern λ_n as:

$$A\dot{\underline{\lambda}}(t) + \frac{U}{b}\underline{\lambda}(t) = \underline{c}\left[\ddot{h}(t) + U\dot{\theta}(t) + b\left(\frac{1}{2} - a\right)\ddot{\theta}(t)\right] \tag{16}$$

where the matrix *A* and the vector $\underline{c}$ are composed of constants determined by the number of induced flow states, *M*, to be included in the analysis. The matrix *A* is given by:

$$A = D + \underline{d}\underline{b}^T + \underline{c}\underline{d}^T + \frac{1}{2}\underline{c}\underline{b}^T \tag{17}$$

where the matrix *D* and vectors $\underline{b}$, $\underline{c}$, and $\underline{d}$ depend on the number of induced flow states. The values of their elements are defined by the following equations:

$$D_{ij} = \begin{cases} \dfrac{1}{2i} & \text{for i} = \text{j} + 1 \\ \dfrac{-1}{2i} & \text{for i} = \text{j} - 1 \\ 0 & \text{for i} \neq \text{j} \pm 1 \end{cases} \tag{18}$$

$$b_i = \begin{cases} (-1)^{i-1} \dfrac{(M+i-1)!}{(M-i-1)!} \dfrac{1}{(i!)^2} & \text{for i} \neq \text{M} \\ (\text{-1})^{\text{i-1}} & \text{for i} = \text{M} \end{cases} \tag{19}$$

$$d_i = \begin{cases} \dfrac{1}{2} \text{ for i} = 1 \\ 0 \text{ for i} \neq 1 \end{cases} \tag{20}$$

$$c_i = \frac{2}{i} \tag{21}$$

5.3 Linear Beam Aerodynamic Forces

In addition to the forces acting on the flap, one must also consider the aerodynamic forces acting on the cantilevered bender as well. When small angles and deflections are assumed to maintain linearity, the aerodynamic force acting on a differential element of the beam is given by the lift force acting on the beam strip element as

$$f(x,t) = f_{L,beam} = \frac{1}{2} \rho_\infty C_{L,beam} w_s U^2 \tag{22}$$

where $C_{L,beam}$ is the effective lift coefficient of the beam element. Assuming that the flow over the beam is approximately steady, the beam element lift coefficient can be approximated by a flat plate using

$$C_{L,beam} = 2\pi \left[\frac{d}{dx} \left(\underline{\phi}(x) \underline{r}(t) \right) + \frac{\underline{\phi}(x) \dot{\underline{r}}(t)}{U} \right] \tag{23}$$

where the bracketed terms approximate the effective angle of attack between the beam element and the incident wind vector including the effects of beam slope and the local velocity of the

beam element. In order to apply the aerodynamic model defined by Eqs. (13) through (23) to the electromechanical system model given by Eqs. (10) through (12), the flap position, $h(t)$, must be related to the beam deflection coordinate $u(x,t)$. This is accomplished by making the substitution given by Eq. (5).

6. Analysis of Limit Cycle Behavior

Above the flutter boundary for the device, experiments show that stable, nonlinear limit cycle oscillations emerge. The limit cycle holds the flutter frequency and amplitude constant over time, leading to a steady state operating condition for a given set of incident flow conditions. The characteristics of this limit cycle behavior and its variation with wind speed are of primary importance to the operation of the flutter power harvester as a generator. The amplitude and frequency of the limit cycle at a given wind speed determine the strain and strain rate in the piezoelectric elements and therefore dictate the electrical output of the system.

In order to analyze the flutter response and steady state operation of the power harvester above the aeroelastic stability boundary, a more complex model must be adopted. While the coupled aeroelastic and electromechanical governing equations derived above are adequate for analyzing the cut-in wind speed of the system, they assume small angles and attached flow to maintain linearity and permit eigenvalue stability analysis. As such, they predict unbounded exponential growth of the oscillation amplitude above the aeroelastic stability boundary. Accurately modeling the limit cycle behavior of the system requires that the model must account for large deflection amplitudes in the mechanical aspects of the model as well as flow separation effects due to large flap angles of attack in the aerodynamics. In order to limit the complexity of

the analysis, it is assumed that linear Euler-Bernoulli beam theory remains applicable and beam hyperextension effects are not significant over the range of wind speeds to be considered. This assumption will be verified experimentally in subsequent sections of the chapter.

6.1 Nonlinear System Model

The nonlinear mechanical model can again be derived using Lagrange equations. The full kinetic energy of the flap can be expressed by generalizing the simplified expression derived using the small angle approximation by Hodges and Pierce (2002) to include large flap deflection angles. The flap kinetic energy is given by

$$T_F = \frac{1}{2} m_F \underline{v}_C \cdot \underline{v}_C + \frac{1}{2} I_C \dot{\theta}^2 \tag{24}$$

where the velocity of the flap center of mass point, *C*, can be expressed as

$$\underline{v}_C = -\hat{i}_2 \dot{h} + \dot{\theta}\left[(1+a)b - (1+e)b\right]\left(\hat{i}_1 \sin\theta - \hat{i}_2 \cos\theta\right) \tag{25}$$

Substituting and applying trigonometric identities, we obtain

$$T_F = \frac{1}{2} m_F \left[\dot{h}^2 - 2(a-e)b\dot{\theta}\dot{h}\cos\theta + (a-e)^2 b^2 \dot{\theta}^2\right] + \frac{1}{2} I_C \dot{\theta}^2 \tag{26}$$

The equation can be simplified by introducing the static unbalance parameter, x_θ, as given by Eq. (3). Making the substitution yields

$$T_F = \frac{1}{2} m_F \left(\dot{h}^2 + 2bx_\theta \dot{\theta}\dot{h}\cos\theta + b^2 {x_\theta}^2 \dot{\theta}^2\right) + \frac{1}{2} I_C \dot{\theta}^2 \tag{27}$$

The flap moment of inertia can be expressed about the hinge point, *P*, using the parallel axis theorem as

$$I_P = I_C + m_F b^2 x_\theta{}^2 \tag{28}$$

Substituting Eq. (28) into Eq. (27) simplifies the flap kinetic energy to

$$T_F = \frac{1}{2} m_F \left(\dot{h}^2 + 2bx_\theta \dot{\theta}\dot{h} \cos\theta \right) + \frac{1}{2} I_P \dot{\theta}^2 \tag{29}$$

The beam and tip mass kinetic energy terms remain unchanged as

$$T_B = \frac{1}{2} \left[\int_{V_S} \rho_S \underline{\dot{u}}^T \underline{\dot{u}} dV_S + \int_{V_M} \rho_M \underline{\dot{u}}^T \underline{\dot{u}} dV_M + \int_{V_P} \rho_P \underline{\dot{u}}^T \underline{\dot{u}} dV_P \right] \tag{30}$$

and

$$T_{tip} = \frac{1}{2} m_{tip} \dot{h}^2 \tag{31}$$

respectively. Thus the total kinetic energy of the system can be expressed by the sum of Eqs. (29) through (31), or

$$T = \frac{1}{2} \left[\begin{array}{l} m_{tip} \dot{h}^2 + m_F \left(\dot{h}^2 + 2bx_\theta \dot{\theta}\dot{h} \cos\theta \right) + I_P \dot{\theta}^2 \\ + \int_{V_S} \rho_S \underline{\dot{u}}^T \underline{\dot{u}} dV_S + \int_{V_M} \rho_M \underline{\dot{u}}^T \underline{\dot{u}} dV_M + \int_{V_P} \rho_P \underline{\dot{u}}^T \underline{\dot{u}} dV_P \end{array} \right] \tag{32}$$

The potential energy terms are determined solely by the beam and therefore remain unchanged as

$$V = \frac{1}{2} \left[\begin{array}{l} \int_{V_S} \underline{S}^T c_S \underline{S} dV_S + \int_{V_M} \underline{S}^T c_M \underline{S} dV_M + \int_{V_P} \underline{S}^T c^E \underline{S} dV_P \\ - \int_{V_P} \underline{S}^T e_P{}^T \underline{E} dV_P - \int_{V_P} \underline{E}^T e_P \underline{S} dV_P - \int_{V_P} \underline{E}^T \varepsilon^S \underline{E} dV_P \end{array} \right] \tag{33}$$

As in the linearized case, the beam deflection coordinate *u(x,t)* can be expressed as a Rayleigh-Ritz modal summation by substituting Eq. (4) into the above relations. Equation (5) is then applied to express the flap heave coordinate, *h(t)*, in terms of the beam coordinates.

When large rotations of the flap are considered, the virtual work due to the flap aerodynamic forces becomes

$$\overline{\delta W}_{flap} = L(t)\left[-\delta h + b\left(\frac{1}{2}+a\right)\delta\theta\cos\theta\right] + D(t)\left[b\left(\frac{1}{2}+a\right)\delta\theta\sin\theta\right] + M_{1/4}(t)\delta\theta \tag{34}$$

where $D(t)$ is the total aerodynamic drag acting on the flap. In the above equation forces acting axially along the beam are assumed to contribute little work and are neglected. After expressing the flap heave deflection in the beam coordinates, the generalized aerodynamic forces acting on the flap heave and pitch degrees of freedom can then be identified as

$$Q_{h,\,flap} = -\underline{\phi}(\ell)^T L(t) \tag{35}$$

$$Q_\theta = b\left(\frac{1}{2}+a\right)\left[L(t)\cos(\theta) + D(t)\sin(\theta)\right] + M_{1/4}(t) \tag{36}$$

As in the linear case, the generalized force due to the beam aerodynamic loading is given by

$$Q_{h,beam} = \int_0^\ell f(x,t)\underline{\phi}(x)^T dx \tag{37}$$

With the kinetic energy, potential energy, and generalized forces defined, the governing equations of the nonlinear system can now be determined. Lagrange's equation is applied to the above relations with beam deflection $\underline{r}(t)$, flap pitch deflection $\theta(t)$, and charge $q(t)$ as the generalized coordinates. As in the linear case, the electrodes of the piezoelectric patches are connected in parallel across a resistive load, and damping effects are approximated by including proportional damping terms. The resulting nonlinear system model is given by

$$\begin{aligned}&\left[M_S + M_M + M_P + m_T\underline{\phi}(\ell)^T\underline{\phi}(\ell)\right]\ddot{\underline{r}} + m_F b x_\theta \underline{\phi}(\ell)^T\cos(\theta)\ddot{\theta} - m_F b x_\theta \underline{\phi}(\ell)^T\sin(\theta)\dot{\theta}^2 \\ &\quad + C_h\dot{\underline{r}} + (K_S + K_M + K_P)\underline{r} - \Theta C_p^{-1} q = -\underline{\phi}(\ell)^T L + \int_0^\ell f\,\underline{\phi}^T dx\end{aligned} \tag{38}$$

$$m_F b x_\theta \underline{\phi}(\ell)\cos(\theta)\ddot{\underline{r}} - m_F b x_\theta \underline{\phi}(\ell)\sin(\theta)\dot{\underline{r}}\dot{\theta} + I_P\ddot{\theta} + C_\theta\dot{\theta} = M_{1/4} + b\left(\frac{1}{2}+a\right)\left[L\cos(\theta)+D\sin(\theta)\right] \tag{39}$$

$$R\dot{q} - C_P{}^{-1}\Theta^T\underline{r} + C_P{}^{-1}q = 0 \tag{40}$$

6.2 Nonlinear Aerodynamic Model

The aerodynamic forces acting on the flap must be calculated using a model that realistically accounts for the nonlinear behavior of the aerodynamics at high angles of attack. In addition, as in the linear regime, the flap motion causes significant unsteady effects on the flow. One such model that has been extensively applied to aeroelastic flutter analysis in the literature the ONERA dynamic stall model developed by Tran and Petot (1981) and Dat and Tran (1983) and later refined by Peters (1985). This semi-empirical model describes the aerodynamic forces acting on a fluttering structure subjected to dynamic stall effects. The dynamic stall phenomenon results from rapid changes in angle of attack that cause separation and reattachment of the flow to be delayed, effectively altering the aerodynamic coefficients (Wickenheiser and Garcia, 2008). These delay effects are modeled with a single lag term incorporated into the linear regime of the aerodynamic force curve and two lag terms applied to the post-stall flow regime. This model represents the aerodynamic force coefficients as

$$C_z = C_{z1} + C_{z2} \tag{41}$$

$$C_{z1} = s_{z1}\overset{*}{\alpha} + s_{z2}\overset{**}{\theta} + s_{z3}\overset{*}{\theta} + C_{z\gamma} \tag{42}$$

$$\overset{*}{C}_{z\gamma} + \beta_1 C_{z\gamma} = \beta_1 a_{0z}\left(\alpha + \overset{*}{\theta}\right) + \beta_2 a_{0z}\left(\overset{*}{\alpha} + \overset{**}{\theta}\right) \tag{43}$$

$$\overset{**}{C}_{z2} + r_1\overset{*}{C}_{z2} + r_2 C_{z2} = -r_2\Delta C_z\big|_\alpha - r_3\Delta\overset{*}{C}_z\Big|_\alpha \tag{44}$$

where the non-dimensional time derivative is defined as

$$\left(\,^{*}\right) = \frac{\partial(\,)}{\partial \tau} \tag{45}$$

with

$$\tau = \frac{Ut}{b} \tag{46}$$

The coefficients s_{z1}, s_{z2}, s_{z3}, r_1, r_2, and r_3 are empirically determined constants and are unique to each aerodynamic force coefficient. The effective angle of attack, α, includes contributions due to pitching and heaving of the flap and is given by

$$\alpha = \theta + \tan^{-1}\left(\frac{\dot{h}}{U}\right) \approx \theta + \frac{\dot{h}}{U} \tag{47}$$

The nonlinear deviation function, ΔC_z, expresses the difference between the linear static aerodynamic force curve and the nonlinear static force curve, with a decrease in force coefficient defined as positive. The full static force curve can therefore be expressed by

$$C_{zs}(\alpha) = a_{0z}\alpha - \Delta C_z(\alpha) \tag{48}$$

The static aerodynamic curves used in the current model are fitted and smoothed curves based on experimental symmetric airfoil aerodynamic data published by Sheldahl and Klimas (1981). The coefficient curves have also been modified so that there are no jump discontinuities for computational considerations. The static aerodynamic force curves are defined by

$$C_L = \begin{cases} 2\pi\alpha & \text{for } \alpha \le 7^\circ \\ -20.7\alpha + 3.252 & \text{for } 7^\circ < \alpha \le 9^\circ \\ 3.067\alpha - 0.495 & \text{for } 9^\circ < \alpha \le 25^\circ \\ 1.1\sin(2\alpha) & \text{for } \alpha > 25^\circ \end{cases} \tag{49}$$

$$C_M = \begin{cases} 0 & \text{for } \alpha \le 7^\circ \\ -0.367\alpha + 0.045 & \text{for } 7^\circ < \alpha \le 25^\circ \\ -0.155\alpha - 0.066 & \text{for } \alpha > 25^\circ \end{cases} \tag{50}$$

$$C_D = 0.3963|\alpha^4| - 2.2584|\alpha^3| + 3.3547|\alpha^2| - 0.0917|\alpha| + 0.0071 \tag{51}$$

where α, the angle of attack, is measured in radians. The coefficients r_1, r_2, and r_3 in Eq. (44) are given by the simplified expressions of Chen (1993) as

$$r_1 = r_{10} + r_{12}(\Delta C_Z)^2 \tag{52}$$

$$r_2 = \left[r_{20} + r_{22}(\Delta C_Z)^2\right]^2 \tag{53}$$

$$r_3 = r_{30} + r_{32}(\Delta C_Z)^2 \tag{54}$$

where the coefficients $r_{10,}$ r_{12}, r_{20}, r_{22}, r_{30}, and r_{32} are empirical constants. These constants were fitted by Chen to match experimental data for an oscillating NACA0012 airfoil at high angles of attack published by McAlister et al. (1982). The coefficients s_{z1}, s_{z2}, s_{z3}, β_1, β_2, and a_{0z} govern the linear portion of the aerodynamic model. These coefficients were derived from unsteady, incompressible flow theory using a single lag state approximation of the Theodorsen function (Chen, 1993). Table 1.3 summarizes the parameters used in the present model.

Table 1.3 Parameters of the nonlinear aerodynamic model (Chen, 1993).

Parameter	*Lift*	*Moment*
a_{0z}	6.28	0
s_{z1}	3.142	-0.786
s_{z2}	1.571	-0.589
s_{z3}	0	-0.786
β_1		0.15
β_2		0.55
r_{10}		0.700
r_{12}		0.150
r_{20}		0.246
r_{22}		0.005
r_{30}		-0.024
r_{32}		0.116

With the necessary aerodynamic coefficients now defined, the aerodynamic lift, drag, and pitching moment acting on the flap can now be calculated using the standard expressions as

$$L = \rho_\infty U^2 bsC_L \tag{55}$$

$$D = \rho_\infty U^2 bsC_D \tag{56}$$

$$M_{1/4} = 2\rho_\infty U^2 b^2 sC_M \tag{57}$$

where the flap is assumed to have a uniform, rectangular planform.

6.3 Nonlinear Beam Aerodynamic Forces

In addition to the aerodynamic forces acting on the flap, the lift and drag forces acting on the beam itself cannot be neglected when large deflections of the beam normal to the flow are considered. Studies (Baker et al. 1967, Juang and Horta, 1987) have shown that there are two components of the drag force that must be considered when a flexible beam vibrates in air. Specifically, these are a force that is proportional to the instantaneous incident wind speed and a

force proportional to the square of the incident wind speed. The total drag force acting on a differential beam strip can then be expressed as

$$f_{D,beam} = C_1 v^2 + C_2 v \tag{58}$$

where v is the instantaneous wind speed incident on the beam. The coefficient C_1 has been shown to be (Baker et al., 1967)

$$C_1 = \frac{1}{2}\rho_\infty C_{D,beam} w_s \tag{59}$$

where $C_{D,beam}$ is the drag coefficient and w_s is the width of the surface normal to the air flow. The form of the coefficient C_2 is not known analytically and must be determined empirically. The lift force acting on the differential beam strip is given by

$$f_{L,beam} = \frac{1}{2}\rho_\infty C_{L,beam} w_s v^2 \tag{60}$$

where $C_{L,beam}$ is the appropriate lift coefficient for the beam section. The instantaneous wind speed incident on the beam must account for both the free stream air flow and the motion of the beam element normal to the flow. Therefore the magnitude of the effective wind speed as a function of time and position along the beam can be expressed by

$$v = \sqrt{U^2 + \left(\phi(x)\dot{r}(t)\right)^2} \tag{61}$$

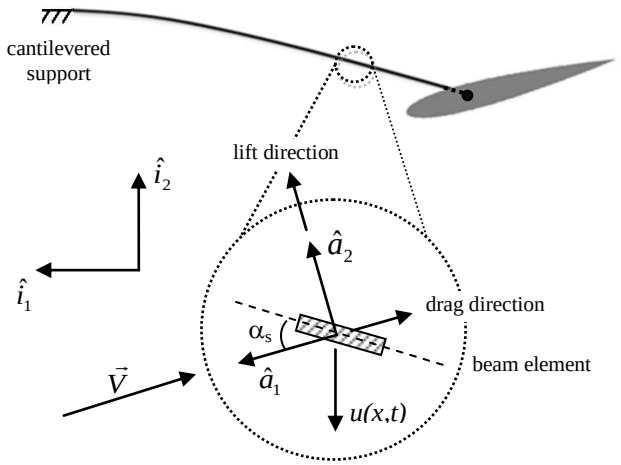

Figure 1.4 Cross section schematic showing coordinate directions for a differential beam strip element.

The total aerodynamic force vector acting the on a differential beam element in the reference frame oriented relative to the incident wind vector is then given by

$$f = -f_{D,beam}\hat{a}_1 + f_{L,beam}\hat{a}_2 \tag{62}$$

with the unit vectors as defined in Figure 1.4. This can rotated into the ground frame by applying the rotation matrix relationship

$$\begin{Bmatrix} \hat{i}_1 \\ \hat{i}_2 \end{Bmatrix} = \begin{bmatrix} \cos(\alpha_s - \theta_s) & \sin(\alpha_s - \theta_s) \\ -\sin(\alpha_s - \theta_s) & \cos(\alpha_s - \theta_s) \end{bmatrix} \begin{Bmatrix} \hat{a}_1 \\ \hat{a}_2 \end{Bmatrix} \tag{63}$$

where α_s is the angle of attack of the differential beam strip and θ_s is the angle of the strip relative to horizontal. In order to simplify the analysis, forces acing along the beam axis were neglected and only the transverse components were considered. This simplification is equivalent to considering the forces acting only in the $\hat{i}_2$ direction. The simplified beam aerodynamic forces can then be expressed in beam deflection coordinate direction as

$$f = -f_{D,beam}\sin(\alpha_s - \theta_s) - f_{L,beam}\cos(\alpha_s - \theta_s) \tag{64}$$

where the *u*-coordinate direction is defined positive down as shown in Figure 1.4. In order to avoid the additional modeling complexity of separated flow incident on the flap downstream due to vortex shedding from the beam, the flow over the beam is assumed to remain steady and attached.

7. Comparison of Model and Experimental Results

7.1 Flutter Boundary Analytic and Experimental Results

The linear system model derived above is applied to the aeroelastic energy harvester apparatus to predict the wind speed and flapping frequency corresponding to the onset of flutter. The first two mode shapes of a cantilevered beam have been found to be adequate to model the piezoelectric bender in the frequency range of interest and are used as the basis functions for the structural model, while four aerodynamic states are included in the unsteady aerodynamic model. The forms of these aerodynamic states are defined by the relations given by Eqs. (16) through (21). The system eigenvalues are determined as a function of the incident wind speed, as shown in Figure 1.5. The flutter boundary is identified as the point where the real part of the one of the eigenvalues becomes positive, representing the transition from stable, decaying oscillations to growing oscillation. The flutter frequency can then be identified from the imaginary part of the eigenvalue at this wind speed. For both the experimental and model results, the resistive load was set to the experimental optimal resistive load, which is given approximately for a weakly coupled piezoelectric system by Guyomar et al. (2005) as

$$R_{opt} = \frac{1}{C_P \omega} \tag{65}$$

where ω is the angular frequency of vibration. Table 1.4 compares the results of the model with measured wind tunnel data.

Figure 1.5 plots the normalized real and imaginary components of the eigenvalues corresponding to the first bending mode of the host structure and the wing rotation mode. These eigenvalues capture much of the qualitative behavior of the flutter boundary. At the onset of flutter, the real parts cross the horizontal axis from negative to positive, representing the transition from a stable damped system in which any disturbance will produce decaying oscillations, to an unstable system with growing oscillations. Qualitatively, this represents the point at which aerodynamic, structural, and electrical damping terms in the system are overcome by destabilizing aerodynamic forces and flutter emerges. The imaginary parts of the normalized eigenvalues show a noticeable convergence trend in the neighborhood of the flutter boundary, suggesting that the frequencies of two degrees of freedom are coalescing as expected, but never fully converge. This behavior is consistent with other published examples of this unsteady aerodynamic model including those of Hodges and Pierce (2002). Turning to the numerical results of Table 1.4, the flutter boundary analysis shows very good agreement with the experimental measurement of the wind speed and oscillation frequency at the onset of flutter. In fact, considering that the resolution of the hot wire anemometer used for the wind speed measurement is 0.1 m/s, the error in the predicted cut-in wind speed is effectively negligible.

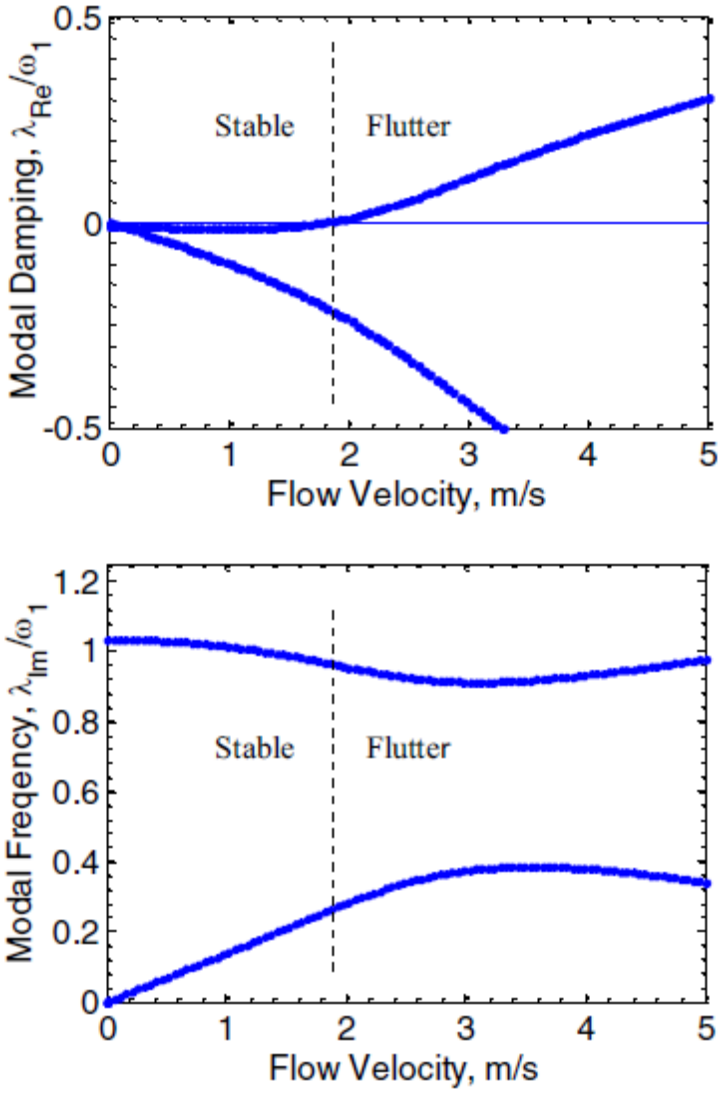

Figure 1.5 Stability analysis plot as a function of wind speed for the aeroelastic energy harvester simulated with N=2 cantilevered beam modes and M=4 unsteady aerodynamic states. The flutter boundary (dashed vertical lines) represents the cut-in wind speed for energy harvesting.

Table 1.4 Comparison of measured and model predicted wind speed and flutter frequency at the flutter boundary. Model results generated using N = 2 beam modes and M = 4 aerodynamic states.

Parameter	*Experimental Result*	*Model Prediction*	*Model Error*
Cut-in Wind Speed	1.9 m/s	1.86 m/s	2.1%
Cut-in Frequency	3.7 Hz	3.69 Hz	0.3%

The use of the first two cantilevered beam modes in the structural model was validated by comparing the predicted cut-in wind speed and flutter frequency for various numbers of modes. Table 1.5 lists the results of this analysis. Not surprisingly, the quality of the model flutter boundary prediction correlates strongly with the prediction of the natural frequency of the first bending mode of the structure. While a single mode approximation significantly over-predicts the first bending natural frequency, and therefore over-predicts the wind speed and flutter frequency at the flutter boundary as well, increasing the number of modes to N = 2 matches the experimental result well. Increasing the number of modes further shows little improvement in the predicted results, indicating that two structural modes are adequate to model the piezoelectric bender.

Table 1.5 Variation in flutter boundary and first structural bending natural frequency with number of cantilevered beam mode shapes included in the analysis. All simulations performed with M = 4 aerodynamic states.

	First Bending Nat. Frequency (Hz)	*Cut-in Wind Speed (m/s)*	*Cut-in Frequency (Hz)*
Experiment	3.8	1.9	3.7
N = 1 mode	4.93	2.83	4.46
N = 2 modes	3.83	1.86	3.69
N = 3 modes	3.81	1.85	3.68
N = 4 modes	3.81	1.85	3.68

As a further validation, the analysis was performed using additional aerodynamic states to ensure that convergence of the finite state, induced flow model had been achieved, as shown in Figure 1.6. The wind speed and frequency of the flutter boundary display little sensitivity to the number of aerodynamic states used in the model beyond M=4 states, indicating that four induced flow states are sufficient to model the unsteady flow over the flap at the onset of flutter.

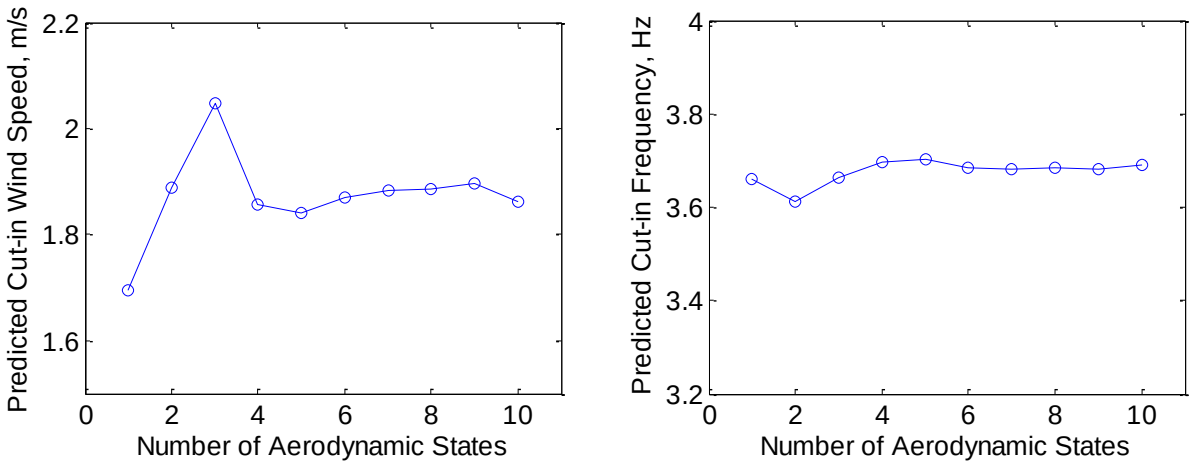

Figure 1.6 Variation in predicted wind speed and flutter frequency at the flutter boundary with number of unsteady aerodynamic states used in the model. All simulations performed with N = 2 cantilevered beam modes.

7.2 Limit Cycle Experimental and Predicted Results

The nonlinear system model derived above was simulated in the time domain using MATLAB's *ode23t.m* numerical integration code to predict the structural and electrical response at wind speeds above the flutter boundary and fit the model to experimental results. The unknown empirical beam aerodynamic drag coefficient from Eq. (58), C_2, is empirically determined for each wind speed using MATLAB's *fminsearch.m* nonlinear optimization tool to fit the system response to the corresponding wind tunnel data. Figure 1.7 shows the variation in the optimized C_2 coefficient with the incident wind speed. Figure 1.8 depicts a typical limit cycle oscillation response simulated at U = 2.6 m/s after the optimization routine has been used to determine the empirical drag coefficient. As expected, after an initial transient, the simulation predicts the system settling into a sinusoidal limit cycle and oscillating in a steady state motion.

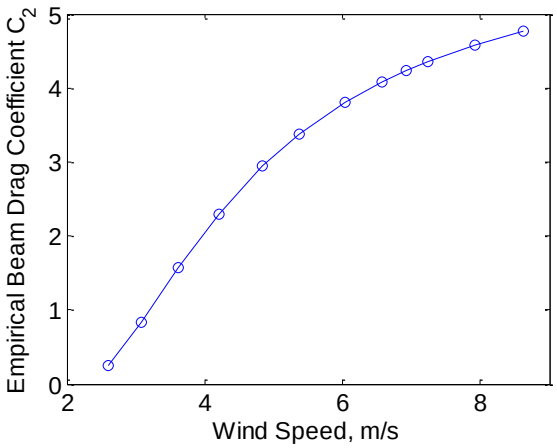

Figure 1.7 Observed variation in empirical beam drag coefficient, $C_{2,}$ with incident wind speed.

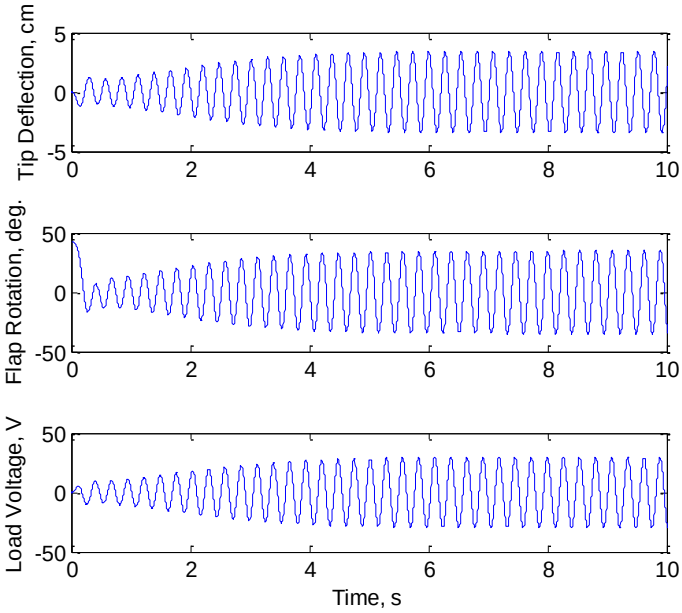

Figure 1.8 Simulated time domain limit cycle oscillation response for bender tip deflection, flap rotation, and voltage through resistive load at wind speed U = 2.6 m/s and optimized load resistance R = 280kΩ.

The transition from a stable, damped system to a flutter limit cycle as the incident wind speed is increased can be described in nonlinear systems terminology as a Hopf bifurcation. These phenomena describe the loss of stability of the system equilibrium point and subsequent emergence of an oscillatory limit cycle as a control parameter is varied and eventually exceeds a

critical value, triggering the bifurcation (Strogatz, 1994). Experimental observations and the model simulations both indicate that the nonlinear dynamics of the aeroelastic energy harvester are governed by a subcritical Hopf bifurcation. This type of Hopf bifurcation leads to an initial condition dependent bistability between fluttering and stable behavior at low wind speeds. Figure 1.9 illustrates that at wind speeds near the flutter boundary, a small initial condition, as shown on the left, leads to oscillations that decay back to the equilibrium, while a larger initial condition, as shown on the right, leads to sustained limit cycle oscillations. This coexistence of a stable equilibrium point and a surrounding limit cycle at the same wind speed is the hallmark of a subcritical Hopf bifurcation.

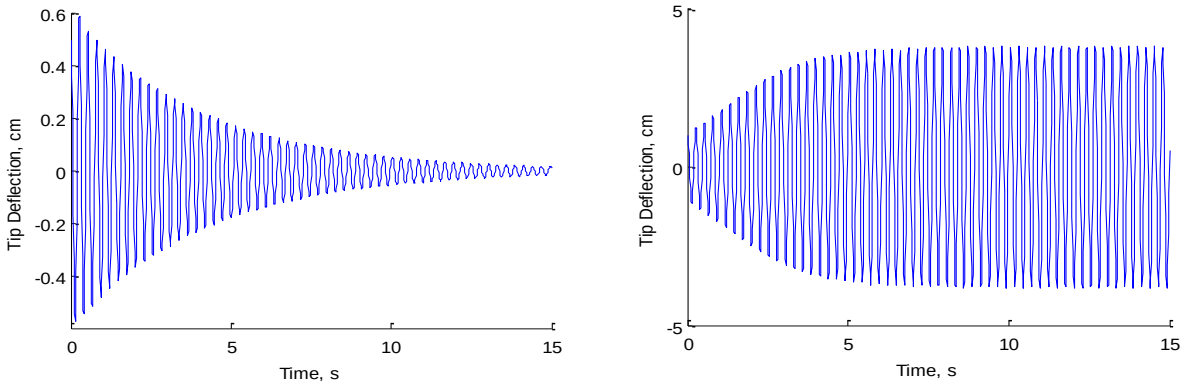

Figure 1.9 Simulated bender tip deflection responses for initial conditions of 0.5 cm (left) and 1.0 cm (right) initial deflection at U=2.35 m/s incident wind speed.

The beam bending and flap rotation amplitudes and frequency of the limit cycle motion vary with the incident wind speed. Figure 1.10 shows limit cycle trajectory plots for several different wind speeds, each calculated beginning from the same initial condition and with the same simulation time. The limit cycle trajectory plots show spiraling elliptical orbit geometry when the flap rotation angle is plotted against the bender tip deflection. The thickness of the ellipse is related to the settling time of the system, while orientation of this ellipse reflects the

phase relationship between the motions of the two degrees of freedom. At lower wind speeds, the plots show a significant phase difference between the flap rotation and bender deflection, as shown by the incline of the major ellipse axis. As the wind speed is increased, however, the major axis of the elliptical orbit approaches the horizontal, implying that the two degrees of freedom are deflecting with a 90 degree phase difference.

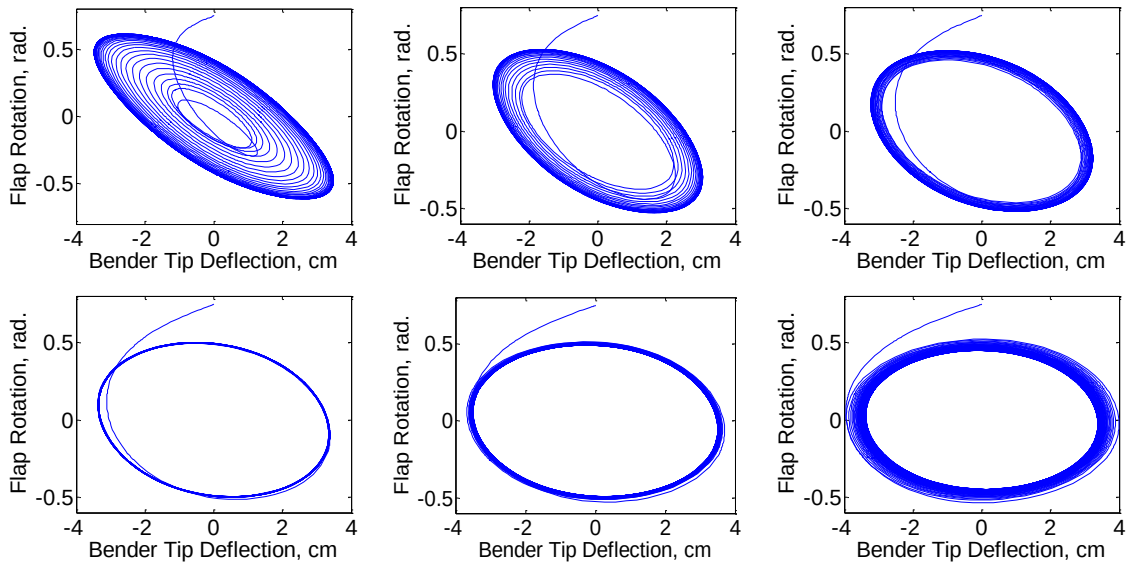

Figure 1.10 Trajectory plots showing transient and limit cycle behaviors for several incident wind speeds simulated over 15 seconds. From left to right in the top row the simulated wind speeds are U = 2.6 m/s, 3.6 m/s, 4.8 m/s, and from left to right in the bottom row U = 6.0 m/s, 6.9 m/s, and 7.9 m/s, respectively.

In order to verify the assumption that the bender deflection remains in the linear range and that the aerodynamic nonlinearities dominate the system, a static deflection test was performed on the bender. The results, shown in Figure 1.11, show that the piezoelectric bender displays an approximately linear force-displacement relationship up to static tip deflections of over 7 cm. The simulated limit cycles shown in Figure 1.10 never exceed 4 cm tip deflection

amplitude, so the limit cycle tip deflections are safely within the linear deflection range of the bender and the linear piezoelectric beam model can be reasonably applied to this system.

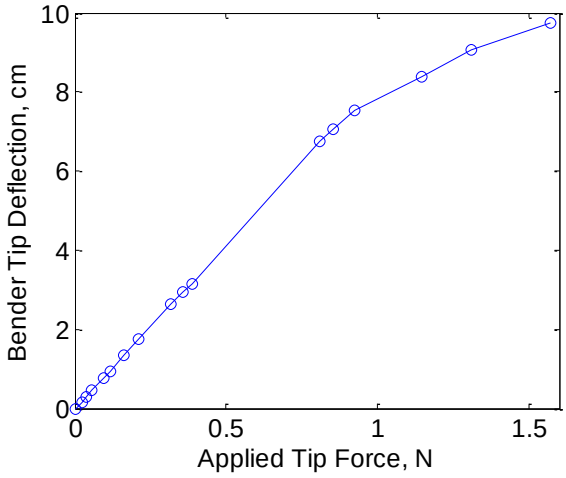

Figure 1.11 Static force-deflection experiment results for the piezoelectric bender.

Figures 1.12 and 1.13 compare the modeled system with the experimental power and frequency data as functions of the incident wind speed. The power output of the aeroelastic energy harvester is shown to vary with the incident wind speed between approximately 0.85 mW and 2.2 mW over the wind speed range tested. While it is important to note that the experimental setup described here was built as a proof of concept only and has not been optimized in any way, this power output would be sufficient for powering low power electronic devices such as wireless sensor nodes. Thus this device could provide a useful means of powering sensing electronics placed in areas where hardwired power is not available and periodically replacing batteries is costly or impractical.

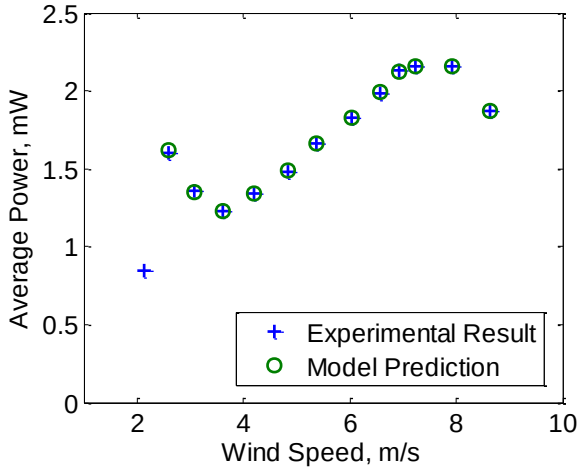

Figure 1.12 Variation in average power through the optimized resistive load with incident wind speed for experimental result and model prediction.

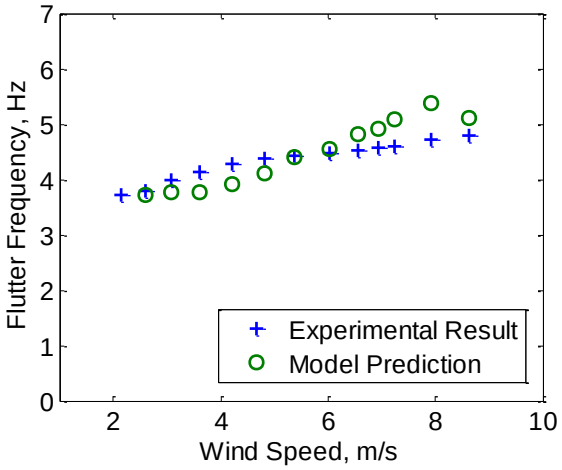

Figure 1.13 Flutter frequency variation with incident wind speed for experimental result and model prediction.

Figure 1.12 shows that the power curve exhibits very close agreement between the model and the experiment throughout the wind speed range with the notable exception that the model fails to predict the first data point. This occurs because the nonlinear aerodynamic model slightly over-predicts the cut-in wind speed. The model result captures the shape of the power curve, showing the first, lower peak at 2.6 m/s that corresponds to the first bending resonance of the

piezoelectric bender, as well as the wider and higher peak at around 7.9 m/s. The location of this peak corresponds to the 90 degree phase difference limit cycle plot at 7.9 m/s as shown in Figure 1.10, suggesting that this condition represents a point of maximum energy transfer from the air flow to the structure and therefore maximum available power for energy harvesting. While the frequency curves show less quantitative agreement, the model still captures the general trend of increasing flutter frequency with wind speed and shows values of the appropriate order of magnitude. The curves differ most significantly in their concavities; the experimental result shows a concave down trend at lower wind speeds and then transitions to a slightly concave up appearance at higher wind speeds while the model shows concave up inflection at across most of the range with the last point dipping slightly.

8. Investigation of Electromechanical Coupling Effects

In addition to estimating the flutter boundary characteristics, nonlinear limit cycle behavior, and power output of the aeroelastic flutter energy harvester, the model can also be used to investigate the effects of the electromechanical coupling and energy harvesting on the system. The piezoelectric energy harvesting extracts energy from the vibrating structure, essentially creating an electromechanical damping effect on the system. In order to examine the influence of this effect on the flutter boundary, the linear system model was analyzed with various resistive load values including very small and very large resistances in addition to the optimized resistive load value. Table 1.6 summarizes the results of this analysis.

As expected, the optimized resistive load extracts the most energy from the system and therefore shows the highest cut-in wind speed and lowest cut-in frequency, both indicative of the

largest electromechanical damping effect. In comparison, the 1Ω load shows the lowest cut-in wind speed because this load approaches a short circuit condition and creates very little electromechanical energy extraction and damping effect. When the load resistance is increased to a very high value, as illustrated by the 100MΩ load, a significant impedance mismatch occurs between the piezoelectric elements and the resistive load which diminishes the ability of energy to flow out of system and into the load resistor, leading to a lower cut-in wind speed.

Table 1.6 Effects of piezoelectric energy harvesting on predicted wind speed and flutter frequency at the flutter boundary.

Resistive Load	*Cut-in Wind Speed (m/s)*	*Cut-in Frequency (Hz)*
1Ω	1.60	3.74
277 kΩ (Optimal Load)	1.86	3.69
100 MΩ	1.62	3.80

Table 1.7 Effects of piezoelectric energy harvesting on simulated steady state flutter limit cycle oscillations at 2.6 m/s.

Resistive Load	*Bender Tip Deflection Amplitude (cm)*	*Flap Rotation Amplitude (deg.)*	*Flutter Frequency (Hz)*
1Ω	4.11	39.6	3.76
280 kΩ (Optimal Load)	3.24	33.2	3.75
100 MΩ	3.93	38.4	3.83

The piezoelectric energy extraction also affects the limit cycle behavior of the system. Table 1.7 summarizes the results of simulations performed for three different resistive loads at 2.6 m/s incident wind speed. In keeping with the results of the flutter boundary analysis, the optimized resistive load extracts the maximum energy from the motion, resulting in the smallest oscillation amplitudes for the tip deflection and flap rotation. The 1Ω and 100MΩ loads show

larger limit cycle amplitudes, again indicating that less energy is being extracted from the motion and less electromechanical damping is present.

The results shown in Tables 1.6 and 1.7 show that the electromechanical coupling has a modest effect on the flutter boundary and limit cycle oscillations, shifting the cut-in wind speed by about 13% and the limit cycle tip deflection amplitude by about 21% when the optimal resistive load and near open circuit conditions are compared. The magnitudes of these shifts are large enough to confirm that it is important to account for the full electromechanical coupling when modeling the system, but not so large that they would pose substantial operational problems in applying the system to charge more complex circuits with inherent electrical dynamics.

9. Conclusions

The problem of designing a piezoelectric energy harvester driven by aeroelastic flutter vibrations had been formulated, solved, and experimentally investigated. The flutter energy harvester necessarily has a minimum cut-in wind speed below which it cannot operate. This parameter would be an important design point for any potential application and would be constrained by size, mass, and material limitations in any practical application. This cut-in wind speed was shown to be predicted by an eigenanalysis of the coupled linear system model. Simultaneously, the power generation characteristics of the device at wind speeds above cut-in are dictated by nonlinear effects in the system including nonlinearities in the mechanism and the aerodynamic loading. A semi-empirical model of the nonlinear electromechanical and aerodynamic system accurately predicted the system power output over a range of wind speeds

and approximated the variation in oscillation frequency with wind speed. The analysis showed that the peak power output of the energy harvester occurs when the beam and flap are deflecting with a 90 degree phase difference. This peak power condition adds a second design consideration for the aeroelastic energy harvester. The design of the energy harvester would depend largely on the characteristics of the expected flow conditions for the intended application. In addition to the cut-in wind speed and coupled system resonant peak, the minor peak in power associated with the first bending resonance of the piezoelectric beam can also be leveraged to enhance the power generation capacity of the energy harvester depending on the nature of the flow environment. In a varying flow application, the energy harvesting system would need to be tailored to have a cut-in wind speed low enough for the device to operate throughout the expected flow speed range and the bender and system resonance peaks placed to maximize power output throughout the range of expected flow conditions. When the energy harvester is applied to a consistent flow condition, however, designing the system to collocate and superpose the bender and system resonances maximizes power output.

REFERENCES

Allen, J. J., and Smits, A. J., 2001, "Energy Harvesting Eel," Journal of Fluids and Structures, 15(3), pp. 629-640.

Anton, S. R., and Sodano, H. A., 2007, "A Review of Power Harvesting Using Piezoelectric Materials (2003-2006)," Smart Materials and Structures, 16, pp. R1-R21.

Baker, W. E., Woolam, W. E., and Young, D., 1967, "Air and Internal Damping of Thin Cantilever Beams," International Journal of Mechanical Sciences, 9, pp. 743-766.

Blevins, R. D., 2001, *Flow Induced Vibration*, Van Nostrand Reinhold Company, New York.

Chen, W. C., 1993, "A Formulation of Nonlinear Limit Cycle Oscillation Problems in Aircraft Flutter," M.S. Thesis, Massachusetts Institute of Technology, Cambridge, MA.

Dat, D., and Tran, C. T., 1983, "Investigation of the Stall Flutter of an Airfoil with a Semi-empirical Model of 2-D Flow," Vertica, 7(2), pp. 73-86.

Dowell, E. H., Curtiss, H.C., Jr., Scanlan, R. H., and Sisto, F., 1980, *A Modern Course in Aeroelasticity*, Sijthoff & Noordhoff, Alphen aan den Rijn, The Netherlands, Chap. 3.

Elvin, N. G., and Elvin, A. E., 2009, "The Flutter Response of a Piezoelectrically Damped Cantilever Pipe," Journal of Intelligent Material Systems and Structures, 20, pp. 2017-2026.

Guyomar, D., Badel, A., Lefeuvre, E., and Richard, C., 2005, "Toward Energy Harvesting Using Active Materials and Conversion Improvement by Nonlinear Processing," IEEE Trans. on Ultrasonics, Ferroelectrics, and Frequency Control, 52(4), pp. 584-595.

Hodges, D. H., and Pierce, G. A., 2002, *Introduction to Structural Dynamics and Aeroelasticity*, Cambridge University Press, Cambridge, UK, Chap. 4.

Juang, J.-N. and Horta, L. G., 1987, "Effects of Atmosphere on Slewing Control of a Flexible Structure," Journal of Guidance ,Control, and Dynamics, 10(4), pp. 387-392.

Khalak, A. and Williamson, C. H. K., 1999, "Motions, Forces, and Mode Transitions in Vortex-Induced Vibrations at Low Mass-Damping," Journal of Fluids and Structures, 13(7-8) , pp. 813-851.

McAlister, K. W., Pucci, S. L., McCroskey, W. J., and Carr, L. W., 1982, "An Experimental Study of Dynamic Stall on Advanced Airfoil Sections Volume 2: Pressure and Force Data," *NASA TM-84245*.

Peters, D. A., 1985, "Toward a Unified Lift Model for Use in Helicopter Rotor Blade Stability Analyses," Journal of the American Helicopter Society, 30(3), pp. 32-43.

Peters, D. A., Karunamoorthy, S., Cao, W. M., 1995, "Finite State Induced Flow Models; Part I; Two Dimensional Thin Airfoil," Journal of Aircraft, 32(2), pp. 313-322.

Pobering, S. and Schwesinger, N., 2004, "A Novel Hydropower Harvesting Device" Proc. 2004 International Conference on MEMS, NANO and Smart Systems, Banff, AL, pp.480–485.

Priya S., Chen C. T., Fye D., and Zahnd J., 2005, “Piezoelectric Windmill: A Novel Solution to Remote Sensing,” Japan. Journal of Applied Physics, 44(3), pp. L104-L107.

Robbins, W. P., Morris, D., Marusic, I., and Novak, T. O., 2006, "Wind-Generated Electricity Using Flexible Piezoelectric Materials," Proc. IMECE 2006, 71, pp. 581-590.

Sheldahl, R. E., and Klimas, P. C., 1981, “Aerodynamic Characteristics of Seven Symmetrical Airfoil Sections Through 180-Degree Angle of Attack for Use in Aerodynamic Analysis of Vertical Axis Wind Turbines,” Sandia National Laboratories Rept. SAND80-2114.

Sodano, H. A., Park, G., and Inman, D. J., 2004, “Estimation of Electric Charge Output for Piezoelectric Energy Harvesting,” Journal of Strain, 40(2), pp. 49-58.

Strogatz, S. H., 1994, *Nonlinear Dynamics and Chaos*, Perseus Books Publishing, Cambridge, MA, Chap. 8.

Taylor, G. W., Burns, J. R., Kammann, S. M., Powers W. B., and Welsh T., R., 2001, “The Energy Harvesting Eel: A Small Subsurface Ocean/River Power Generator,” IEEE J. Oceanic Eng., 26(4), pp. 539–47.

Theodorsen, T. 1934. “General Theory of Aerodynamic Instability and the Mechanism of Flutter,” NACA Report No. 496, pp. 413-433.

Tran, C. T. and Petot, D., 1981, “Semi-Empirical Model for the Dynamic Stall of Airfoils in View of Application to the Calculated Responses of a Helicopter in Forward Flight,” Vertica, 5(1), pp. 35-53.

van Oudheusden, B. W., 1996, “Rotational One-Degree-of-Freedom Galloping in the Presence of Viscous and Frictional Damping,” Journal of Fluids and Structures, 10, pp. 673-689.

Wickenheiser, A. M. and Garcia, E., 2008, “Optimizing of Perching Maneuvers Through Vehicle Morphing,” Journal of Guidance, Control, and Dynamics, 31(4), pp. 815-823.

This chapter originally appeared as:

Bryant, M., and Garcia, E., 2011, "Modeling and Testing of a Novel Aeroelastic Flutter Energy Harvester," Journal of Vibrations and Acoustics, 133, 011010. Reprinted by permission of ASME.

CHAPTER 2
AEROELASTIC FLUTTER ENERGY HARVESTER DESIGN: SENSITIVITY OF THE DRIVING INSTABILITY TO SYSTEM PARAMETERS

1. Abstract

This chapter examines the design parameters affecting the stability characteristics of a novel fluid flow energy harvesting device powered by aeroelastic flutter vibrations. The energy harvester makes use of a modal convergence flutter instability to generate limit cycle bending oscillations of a cantilevered piezoelectric beam with a small flap connected to its free end by a revolute joint. The critical flow speed at which destabilizing aerodynamic effects cause self-excited vibrations of the structure to emerge is essential to the design of the energy harvester because it sets the lower bound on the operating wind speed and frequency range of the system. A linearized analytic model of the device that accounts for the three-way coupling between the structural, unsteady aerodynamic, and electrical aspects of the system is used to examine tuning several design parameters while the size of the system is held fixed. The effects on the aeroelastic system dynamics and relative sensitivity of the flutter stability boundary are presented and discussed. A wind tunnel experiment is performed to validate the model predictions for the most significant system parameters.

2. Introduction

Piezoelectric energy harvesting has received considerable attention as a means to power wireless electronics and sensors in applications where the finite energy capacity of a battery is undesirable. This research has predominately focused on harvesting energy from existing

vibrating structures by exciting cantilevered beams through base excitation (Anton and Sodano, 2007). This approach imposes inherent limitations on the applications of piezoelectric energy harvesting, especially in remote environments where a suitable source of ambient vibrations may not be present. One solution to this limitation is to design energy harvesting systems that can be excited to vibrate through interaction with wind or other available fluid flows. Such a device could enable battery independent wireless electronics anywhere ambient fluid flows are available. Potential applications range from powering health monitoring sensors on aircraft or bridges, to tracking tags on swimming or flying animals, to sensors inside pipelines or water systems. Bryant and Garcia (2011) recently proposed, modeled, and tested a novel energy harvester driven by aeroelastic flutter oscillations of a piezoelectric beam with a simple flap attached to the beam tip.

While several other groups have investigated harnessing vibrations created by fluid-structure interaction to drive piezoelectric energy harvesting structures, the approach of Bryant and Garcia is unique because of the instability mechanism that generates the oscillations. Previous researchers have proposed devices excited by vortices shed from upstream bluff bodies in both flowing liquids (Allen and Smits, 2001, Taylor et al. 2001, Pobering and Schwesinger, 2004) and gaseous flows (Robins et al., 2008). Another study has examined a piezoelectric cantilever with a bluff body affixed directly to the free end of the beam (Kwon, 2010). The approach of Bryant and Garcia, however, generates self-excited vibrations by making use of a modal convergence flutter instability. Modal convergence flutter is distinguished from other types of aeroelastic vibration such as vortex induced vibration (Khalak and Williamson, 1999) or unimodal galloping (van Oudheusden, 1996) due to the interaction of multiple, coupled structural modes that are driven to coalescence by aerodynamic forces (Dowell et al., 1980, Hodges and

Pierce, 2002). Aeroelastic instabilities are characterized by a critical set of flow conditions that define the stability boundary for the system, or the point at which the instability appears and flutter oscillations emerge. This condition represents the point at which the fluid flow transitions from providing a dissipative effect on the system to transferring energy into the structure and producing growing oscillations. The flutter energy harvester takes advantage of nonlinearities in the aerodynamics and mechanical system to establish bounded limit cycle oscillations and thereby cyclically strain the piezoelectric beam over a broad range of wind speeds.

This chapter further investigates the aeroelastic energy harvester concept by examining the sensitivity of the driving aeroelastic instability to several design parameters. Existing literature has examined traditional piezoelectric vibration energy harvesting at length and has already investigated tuning and optimization of many aspects including beam geometry (Dietl and Garcia, 2010), and power electronics (Guyomar et al., 2005, Wickenheiser and Garcia, 2010), so this investigation focuses on the novel aspect of this device, the aeroelastic excitation. In particular, we examine the relationships between several system design parameters and the "cut-in wind speed", or minimum wind speed required for self-sustained flutter oscillation of the energy harvester. The complex nature of the flutter instability opens the design space to more parameters than simpler energy harvesting mechanisms such as base excitation. The parameters considered in this study are chosen based on a fixed size of the system and its components.

3. System Model and Problem Formulation

3.1. System Configuration

The aeroelastic flutter energy harvester is excited by a two degree of freedom aeroelastic instability that produces limit cycle oscillations of the system over a range of wind speeds. The necessary degrees of freedom are created by the bending deflection of the cantilevered piezoelectric beam, providing a heaving degree of freedom, along with the rotation of the flap about a hinge joint, providing a pitching degree of freedom. These two degrees of freedom are mechanically coupled by a mass unbalance in the flap created by the chordwise separation of the hinge axis and the flap center of mass. The flap static unbalance parameter, x_θ, quantifies this coupling effect in terms of the dimensionless center of mass location, e, and dimensionless hinge location, a, as

$$x_\theta = e - a \tag{1}$$

This system can be represented schematically by the lumped mass system shown in Figure 2.1. This system is based on the two degree of freedom wing section model often employed in the aeroelasticity literature, but has been modified to include the electromechanical coupling of the piezoelectric beam and the non-rotating beam tip mass. One possible embodiment of this flutter energy harvester concept is the simple wind tunnel experiment shown in Figure 2.2. This device serves as the example system under consideration herein and is further described in Section 4.

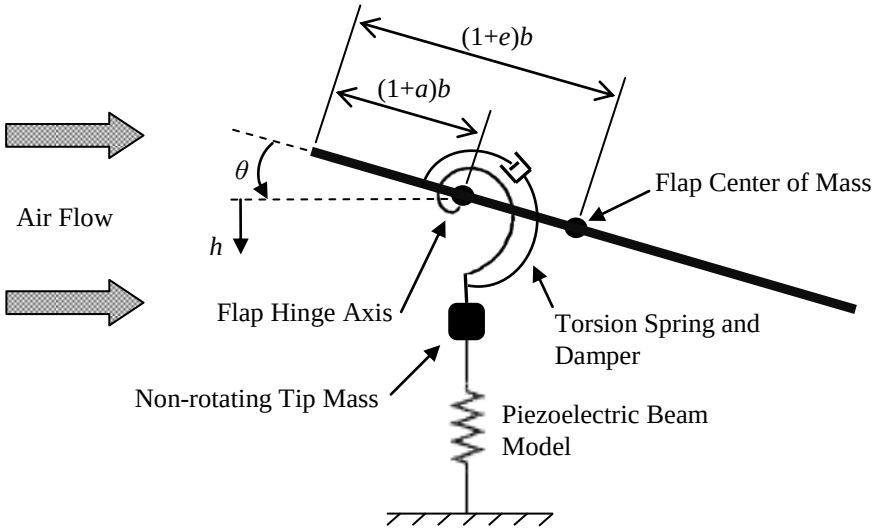

Figure 2.1 Aeroelastic flutter energy harvester schematic with coordinates defined and flap hinge and center of mass positions expressed in terms of the flap semi-chord, *b*.

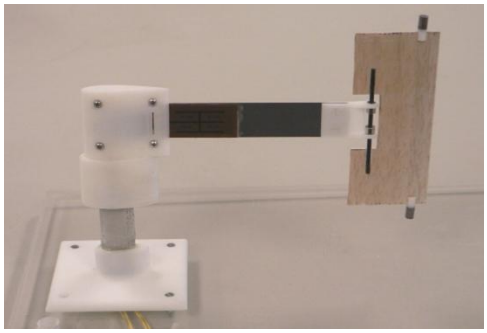

Figure 2.2 Photograph of the aeroelastic flutter energy harvester wind tunnel experiment.

3.2. Nonlinear System Model

Bryant and Garcia have shown that the flutter energy harvester can be modeled by applying Hamilton's principle to derive a system of equations that describe the coupled dynamics of the aeroelastic and electromechanical aspects of the system (2011). This approach

models the piezoelectric beam according to a Rayleigh-Ritz modal summation technique (Sodano, Park, and Inman, 2004, Hagood, Chung, and von Flotow, 1990) and represents the flap using the two dimensional wing section model that is commonly applied in the aeroelasticity literature (Hodges and Pierce, 2002). The beam deflection coordinate, $u(x,t)$ is then given in terms of the assumed beam mode shapes and a temporal coordinate by

$$u(x,t) = \sum_{i=1}^{N} \phi_i(x) r_i(t) = \underline{\phi}(x)\underline{r}(t) \tag{2}$$

where $\phi_i(x)$ is the beam mode shape, $r_i(t)$ is the temporal coordinate, and N is the number of beam mode shapes necessary to represent the system. This method is then used to express the flap heave deflection coordinate, $h(t)$, in terms of the beam coordinates as

$$h(t) = u(\ell,t) = \underline{\phi}(\ell)\underline{r}(t) \tag{3}$$

where ℓ is the length of the composite beam, and $h(t)$ is measured from the flap revolute joint. Bryant and Garcia give the coupled system model in terms of the beam deflection coordinate $\underline{r}(t)$, flap rotation angle $\theta(t)$, and output charge $q(t)$. When large flap rotation angles are considered and the piezoelectric outputs are connected to a resistive load, this model is given by

$$\begin{aligned}&\left(M_S + M_M + M_P + \left(m_{NR} + m_F\right)\underline{\phi}(\ell)^T \underline{\phi}(\ell)\right)\ddot{\underline{r}} + m_F b x_\theta \underline{\phi}(\ell)^T \cos(\theta)\ddot{\theta} - m_F b x_\theta \underline{\phi}(\ell)^T \sin(\theta)\dot{\theta}^2 \\ &+ C_h \dot{\underline{r}} + (K_S + K_M + K_P)\underline{r} - \Theta C_p{}^{-1} q = -\underline{\phi}(\ell)^T L + \int_0^\ell f\,\underline{\phi}^T dx\end{aligned} \tag{4}$$

$$\begin{aligned}&m_F b x_\theta \underline{\phi}(\ell)\cos(\theta)\ddot{\underline{r}} - m_F b x_\theta \underline{\phi}(\ell)\sin(\theta)\dot{\underline{r}}\dot{\theta} + I_P\ddot{\theta} + C_\theta\dot{\theta} + K_\theta\theta \\ &= M_{1/4} + b\left(\frac{1}{2} + a\right)\left[L\cos(\theta) + D\sin(\theta)\right]\end{aligned} \tag{5}$$

$$R\dot{q} - C_P{}^{-1}\Theta^T \underline{r} + C_P{}^{-1} q = 0 \tag{6}$$

where the matrices M_S, M_M, and M_P, are the mass matrices representing the substrate, epoxy matrix, and piezoelectric material respectively, and the matrices K_S, K_M, and K_P are the substrate, epoxy matrix, and piezoelectric stiffness matrices respectively. The terms m_{NR} and m_F are the non-rotating beam tip mass and flap mass, respectively, I_P is the flap mass moment of inertia about the hinge axis, and b is the flap semichord. The C_h and C_θ terms are viscous damping coefficients to approximate losses in the heave and pitch degrees of freedom respectively, $L(t)$ is the lift force acting on the flap, $D(t)$ is the drag force acting on the flap, $M_{1/4}(t)$ is the aerodynamic pitching moment acting at the flap quarter chord, and $f(x,t)$ is the distributed aerodynamic load acting on the piezoelectric beam. The term R is the resistive load, C_P is the piezo capacitance matrix, and Θ is the electromechanical coupling matrix.

3.3 Linearized System Model

In order to determine the flow conditions at which the onset of flutter occurs for a given energy harvester configuration, it is convenient to linearize the nonlinear system model given by Eqs. (4) through (6) above by assuming that the angle θ is small. This linearization about the small angle condition allows for an eigenvalue stability analysis to be performed and the flutter stability boundary to be identified. The linearized system model can be shown to be

$$\begin{aligned}&\left(M_S + M_M + M_P + \left(m_{NR} + m_F\right)\underline{\phi}(\ell)^T \underline{\phi}(\ell)\right)\ddot{\underline{r}} + m_F b x_\theta \underline{\phi}(\ell)^T \ddot{\theta} + C_h \dot{\underline{r}} + (K_S + K_M + K_P)\underline{r} - \Theta C_p{}^{-1} q \\ &= -\underline{\phi}(\ell)^{\mathrm{T}} \mathrm{L} + \int_0^\ell f \underline{\phi}^{\mathrm{T}} \mathrm{dx}\end{aligned} \tag{7}$$

$$m_F b x_\theta \underline{\phi}(\ell)\ddot{\underline{r}} + I_P \ddot{\theta} + C_\theta \dot{\theta} + K_\theta \theta = M_{1/4} + b\left(\frac{1}{2} + a\right)L \tag{8}$$

$$R\dot{q} - C_P{}^{-1}\Theta \underline{r} + C_P{}^{-1} q = 0 \tag{9}$$

3.4 Aerodynamic Model

In order to accurately predict the aerodynamic forces acting on the flap, an unsteady aerodynamic model that accounts for the circulatory and non-circulatory aerodynamic effects acting on the system must be applied. These unsteady effects arise due to the of the pitching and heaving motions of the flap and ensuing vortex shedding from the trailing edge of the flap, as well as the "added mass" effects due to accelerations of the flap. The finite state, induced flow model of Peters et al. provides such a representation of the unsteady aerodynamic lift force, $L(t)$, and pitching moment, $M_{1/4}(t)$, acting on the flap for small angles of attack and inviscid, incompressible flows using a time domain, state-space approach that can be derived from first principle fluid mechanics. The reader is referred to Peters et al. for the details of the derivation of this model (1995) and Bryant and Garcia (2011) for its application to this flutter energy harvester system.

The deflecting piezoelectric beam is also subject to aerodynamic forces that affect the dynamics of the aeroelastic energy harvesting system. In keeping with the small angle linearization approximation for stability analysis discussed above, small beam deflections can be assumed at the onset of the flutter instability. The aerodynamic force distribution, $f(x,t)$, acting along the beam is approximated by assuming that a differential beam strip element acts as a flat plate in steady flow, with an effective angle of attack that includes contributions due to the beam slope and relative velocity of the beam with respect to the free stream flow (Bryant and Garcia, 2011).

4. System Setup

The aeroelastic energy harvesting device configuration considered in the present study is shown schematically in Figure 2.3. Based on the aeroelastic energy harvester described in prior work by Bryant and Garcia (2011), the system design modeled here uses a cantilevered elastic 301 stainless steel beam with a pair of MIDE Quickpack QP10N piezoelectric patches laminated to the beam root. The root of the beam is assumed to be clamped to ground, while a rigid flat plate flap is hinged to the tip of the piezoelectric beam by a revolute joint. This arrangement creates an aeroelastic system with two coupled degrees of freedom that exhibit a modal convergence flutter instability and limit cycle oscillations when a critical wind speed is exceeded. The aeroelastic flutter phenomenon creates cyclic bending deformations of the beam, straining the piezoelectric patches and tranducing the mechanical strain into electrical energy. For consistency, the same piezoelectric beam configuration is used in all cases, while the parameters of the flap and beam tip are varied within the constraint that the size of the system and its components are held constant. The resistive load connected to the electrodes of the piezoelectric patches is set to the optimal value for maximum power extraction. For a low coupling system, this value is given by

$$R_{opt} = \frac{1}{C_P \omega} \tag{10}$$

where ω is the angular frequency of vibration (Guyomar et. al, 2005). The fixed dimensions, mechanical parameters, and electromechanical properties of the piezoelectric beam and flap used throughout all parameter analyses are shown in Table 2.1.

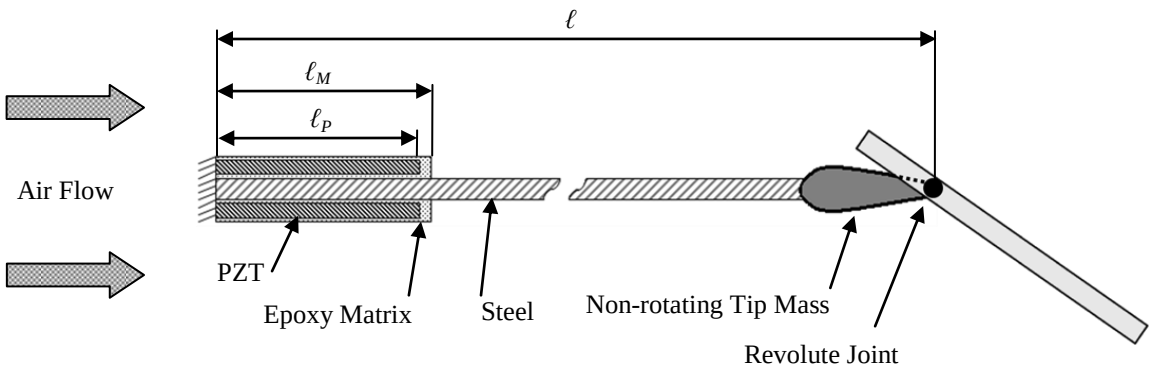

Figure 2.3 Schematic of the aeroelastic energy harvester showing the composite beam geometry.

Table 2.1 Fixed dimensions and parameters of the aeroelastic energy harvester model.

Parameter	*Symbol*	*Value*	*Units*
Physical:			
flap span	s	12.0	cm
flap semichord	b	3.0	cm
beam length	ℓ	12.9	cm
beam width	w	2.63	cm
beam substructure thickness	t_s	0.381	mm
PZT layer thickness	t_P	0.254	mm
PZT patch length	ℓ_P	4.60	cm
PZT patch width	w_P	2.06	cm
epoxy matrix layer thickness	t_m	0.0254	mm
epoxy matrix length	ℓ_m	4.90	cm
epoxy matrix width	w_m	2.53	cm
beam substructure density	ρ_S	7850	kg/m^3
PZT density	ρ_P	7700	kg/m^3
epoxy matrix density	ρ_m	2150	kg/m^3
Mechanical:			
beam substructure stiffness	c_S	212	GPa
PZT stiffness, open circuit	c^E	67	GPa
epoxy matrix stiffness	c_M	2.5	GPa
Electromechanical:			
piezoelectric constant	d_{31}	−190	pm/V
constant strain permittivity	ε^S	15.93	nF/m

5. Parameter Variation Studies

The model described above is applied to study the effects of several design parameters on the cut-in wind speed of the aeroelastic flutter energy harvester. In this modal convergence flutter system, the heave degree of freedom is provided by the flexible piezoelectric beam, while the pitch degree of freedom is created by the rotating hinge joint. Unlike a typical aircraft wing, which is the aeroelastic system commonly studied in the literature, the zero-wind-speed pitch natural frequency of the energy harvester is lower than that of the heave degree of freedom. With the hinge axis located forward of the aerodynamic center, increasing wind speed leads to an aerodynamic "weather cocking" effect that increases the effective stiffness of the hinge joint. This drives the natural frequency of the pitch mode higher, while the pitch-heave coupling created by the static mass unbalance in the flap pulls the natural frequency of the heave mode lower, allowing the two modal frequencies to converge and flutter to emerge. The mechanics of the flutter phenomenon thus reveal several quantities that affect the wind speed at which the flutter instability occurs, including the zero-wind-speed natural frequencies of the pitch and heave degrees of freedom, the degree of coupling between the two modes, and the extent of aerodynamic stiffening of the hinge joint due to weather cocking. Variations in the system design parameters are used to change these quantities and alter the cut-in wind speed of the system. The specific parameters that will be considered in the subsequent sections of this paper are:

1. non-rotating beam tip mass
2. flap mass
3. flap mass moment of inertia

4. flap hinge natural frequency

5. chordwise flap center of mass (CoM) location

6. chordwise flap hinge location

Table 2.2 lists the baseline parameters for the system that are used throughout the parameter variation study, while Table 2.3 lists the individual parameters that are altered in each section and the ranges of their respective values.

Table 2.2 Baseline parameters of the aeroelastic energy harvester.

Parameter	*Symbol*	*Value*	*Units*
non-rotating tip mass	m_{NR}	3.5×10^{-3}	kg
flap mass	m_F	6.4×10^{-3}	kg
flap mass moment of inertia	I_P	0.017	kg·cm^2
flap hinge location	a	−0.53	unitless
flap center of mass location	e	−0.27	unitless
flap hinge stiffness	K_θ	0	N·m/rad

Table 2.3 Parameter variations performed.

Parameter	*Symbol*	*Value*	*Units*
1. Non-rotating tip mass study: non-rotating tip mass	m_{NR}	0 to 0.020	kg
2. Flap Mass study flap mass	m_F	0 to 0.035	kg
3. Flap Moment of Inertia Study flap mass moment of inertia	I_P	0 to 0.10	kg·cm^2
4. Hinge Natural Frequency Study: flap hinge stiffness	K_θ	0 to 1.3	N·cm/rad
5. Flap CoM Location Study dimensionless CoM position	e	−0.5 to 0.18	unitless
6. Flap Hinge Location Study dimensionless hinge position	a	−1 to −0.50	unitless

5.1. Sensitivity to Non-rotating Beam Tip Mass

The mass attached to the free end of the beam that does not rotate with the hinged flap is quantified by the non-rotating tip mass parameter, m_{NR}. This parameter appears in the inertia term of the beam force balance equation given by Eq. (7), and affects the zero-wind speed bending natural frequencies of the piezoelectric beam as shown in Figure 2.4. The non-rotating tip mass is nondimensionalized by the total system mass, which includes the masses of the piezoelectric beam, flap, and tip mass in this and subsequent plots.

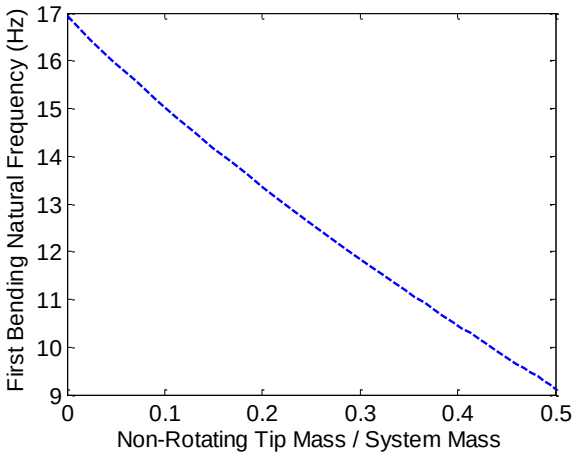

Figure 2.4 Effect of varying non-rotating beam tip mass on the first bending natural frequency of the piezoelectric beam.

Figure 2.5 plots the effects of varying the dimensionless non-rotating beam tip mass on the cut-in wind speed of the aeroelastic energy harvester, while Figure 2.6 shows the effects on the cut-in frequency of the system. Increasing the non-rotating tip mass causes the both the cut-in wind speed and cut-in frequency to decrease monotonically throughout the range of tip masses simulated. In addition, the results for both cut-in frequency and wind speed show a slight

upward concavity as the tip mass is increased. Model predictions are shown for several values of the hinge damping ratio, $\zeta_{\theta,}$ including undamped, $\zeta_\theta = 0.2$, and $\zeta_\theta = 0.4$ cases. Physically, this viscous damping approximates the energy dissipation due to losses in the bushings or ball bearings in the revolute joint. Understanding the sensitivity of the cut-in wind speed and frequency to this parameter is important because practical bearings will always introduce some dissipation into the hinge. Increasing the hinge damping ratio shifts the cut-in wind speed and frequency results upward only slightly, but has little effect on the shape of the curve.

These trends correspond closely with the variation in the first bending natural frequency of the piezoelectric beam with tip mass, as shown by Figure 2.4. In fact, when the cut-in wind speed and cut-in frequency are plotted against the first beam natural frequency, as shown in Figures 2.7 and 2.8, respectively, clear linear correlations are observed in both cases, with increasing natural frequencies corresponding to increasing cut-in wind speeds and cut-in frequencies. The strong dependence of the cut-in conditions on the beam natural frequency is not surprising when the nature of the flutter instability present in this system is considered. By adding tip mass and decreasing the beam natural frequency, this convergence occurs at a lower wind speed and lower frequency, leading to the decreasing cut-in wind speeds and frequencies observed here.

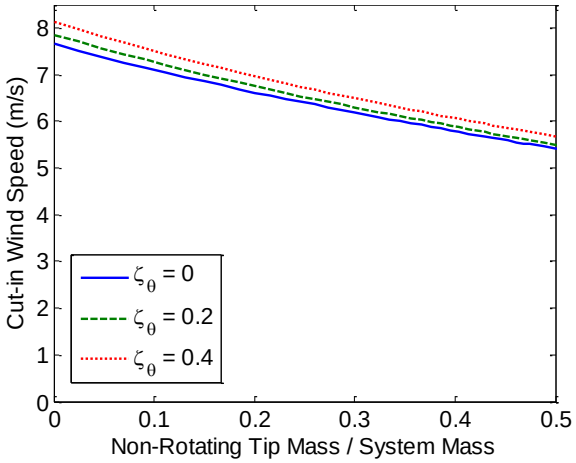

Figure 2.5 Change in cut-in wind speed as a function of beam non-rotating tip mass.

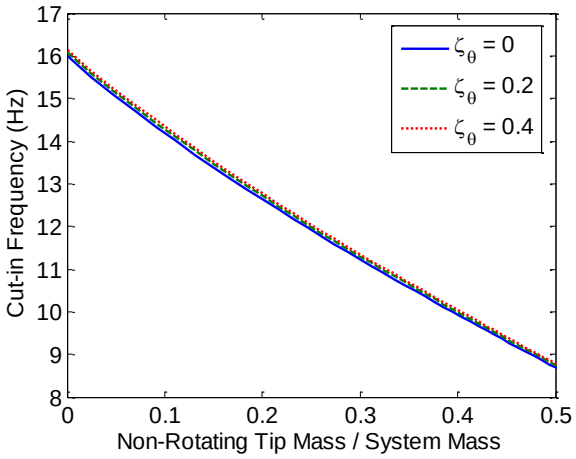

Figure 2.6 Change in cut-in frequency as a function of beam non-rotating tip mass.

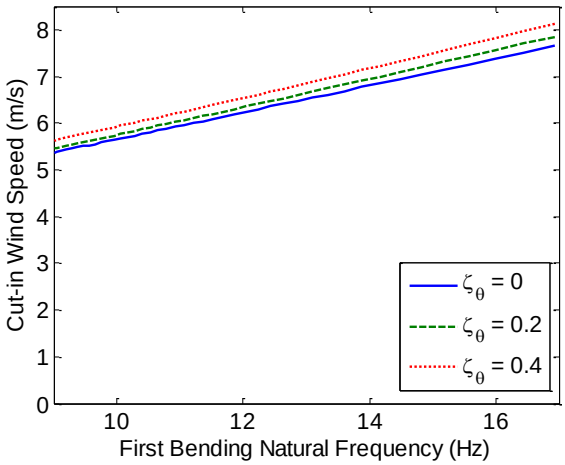

Figure 2.7 Effect of varying beam first bending natural frequency due to changes in non-rotating tip mass on the cut-in wind speed.

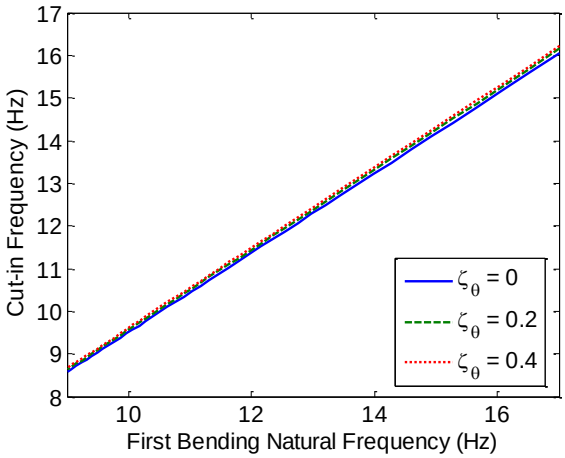

Figure 2.8 Effect of varying beam first bending natural frequency due to changes in non-rotating tip mass on the cut-in frequency.

5.2. Sensitivity to Flap Mass

Like the non-rotating tip mass parameter described above, the mass of the hinged flap, m_F, also affects the bending natural frequencies of the piezoelectric beam by contributing to the total tip mass attached to the beam. Accordingly, the beam bending natural frequency variation due to changes in the non-rotating tip mass and the flap mass shown by Figures 2.4 and 2.9, respectively, show identical trends. In addition, the coupling term, $m_F b x_\theta \underline{\phi}(\ell)$, between the pitch (flap rotation) and heave (beam bending) modes of the system that appears in the angular acceleration term of Eq. (7) and the linear acceleration term of Eq. (8) is proportional to the flap mass. By changing both the beam natural frequencies and the pitch-heave coupling, the flap mass parameter creates a more pronounced effect on the cut-in characteristics of the aeroelastic system. This flap mass parameter is expressed in nondimensional form through normalization by the total system mass.

As the flap mass approaches zero, the cut-in wind speed rapidly increases. With decreasing flap mass, the pitch-heave coupling proportionally decreases and the fundamental beam natural frequency increases according to the curve shown in Figure 2.9. Qualitatively, the higher first natural frequency of the beam produces a larger zero wind speed frequency separation between the heave and pitch modes of the system, meaning that higher aerodynamic forces are required to drive the frequencies to converge. In addition, the weakened coupling between the pitch and heave modes also shifts the flutter instability point to higher and higher wind speeds. The superposition of these effects leads to a substantial variation in cut-in wind speed and frequency with flap mass, as shown by the curves in Figures 2.10 and 2.11 respectively. The cut-in wind speed achieves a minimum value of 5.4 m/s at a dimensionless flap mass of 0.43 (m_F = 0.013 kg) before increasing slightly as the flap mass is further increased, while the cut-in frequency decreases throughout the range. Notably, for dimensionless flap masses greater than about 0.65 (m_F = 0.033 kg), a static divergence instability rather than flutter occurs, placing an upper bound on the range of this parameter.

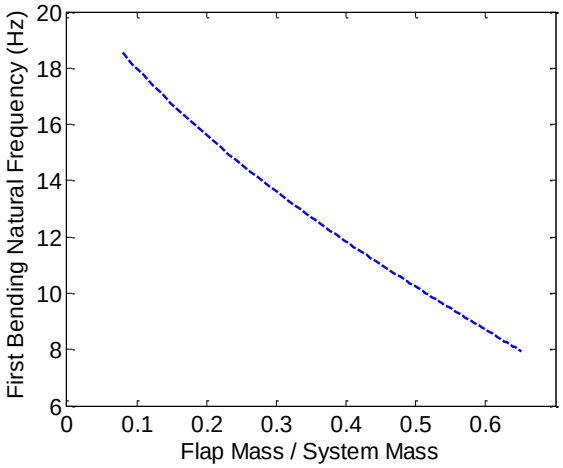

Figure 2.9 Effect of varying flap mass on the first bending natural frequency of the piezoelectric beam.

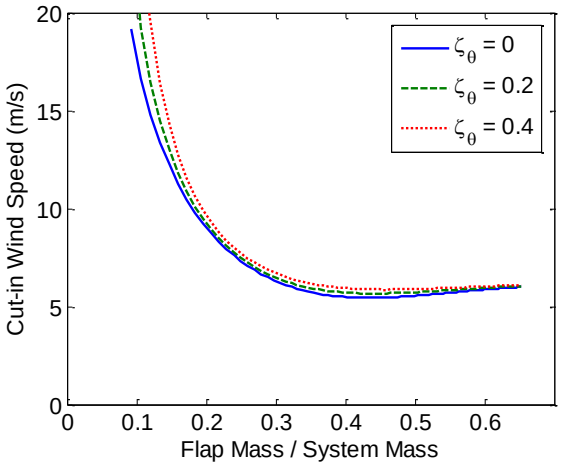

Figure 2.10 Change in cut-in wind speed as a function of flap mass.

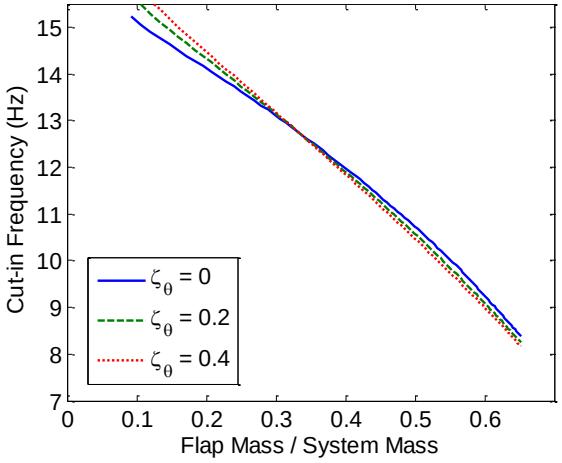

Figure 2.11 Change in cut-in frequency as a function of flap mass.

5.3. Sensitivity to Flap Mass Moment of Inertia

In addition to the translational motion experienced by the flap due to the heave degree of freedom, the flap also rotates about the hinge joint. Therefore we expect its mass moment of inertia, I_P, to be a significant parameter in the system. The aerodynamic forcing terms of Eq. (8) serve to stiffen the flap hinge joint as the incident wind speed is increased, driving the natural frequency of the pitch degree of freedom higher and toward convergence with the heave natural

frequency. Altering the mass moment of inertia of the flap changes the response of the pitch natural frequency to the incident wind speed, with a larger moment of inertia weakening the aerodynamic "weather cocking" effect on the flap. Thus, a larger moment of inertia equates to a lower rate of increase in pitch natural frequency with wind speed.

The flap moment of inertia is expressed in nondimensional form by

$$I_P^* = \frac{2I_P}{\pi\rho_\infty(1-a)^4 b^4 s} \tag{11}$$

where I_P^* is the dimensionless moment of inertia of the flap. This expression nondimensionalizes the flap moment of inertia by the moment of inertia of a cylinder of air centered on the flap hinge line with its radius defined by trailing edge of the flap and length equal to the flap span (Andersen, Pesavento, and Wang, 2005). Figure 2.12 shows that a higher dimensionless flap moment of inertia shifts the cut-in wind speed to faster airflows throughout most of the range tested. Notably, static divergence rather than flutter oscillations occur for dimensionless flap moment of inertia below 0.14 (I_P = 1.4×10^{-3} kg·cm^2), and a weak minimum occurs near 0.75 (I_P = 7.0×10^{-3} kg·cm^2) at a cut-in wind speed of 5.0 m/s. The cut-in frequency, plotted in Figure 2.13, shows the opposite trend, with higher flap moments of inertia leading to lower cut-in frequencies, showing that the pitch-heave coupling is pulling the heave natural frequency lower when more flap inertia is present.

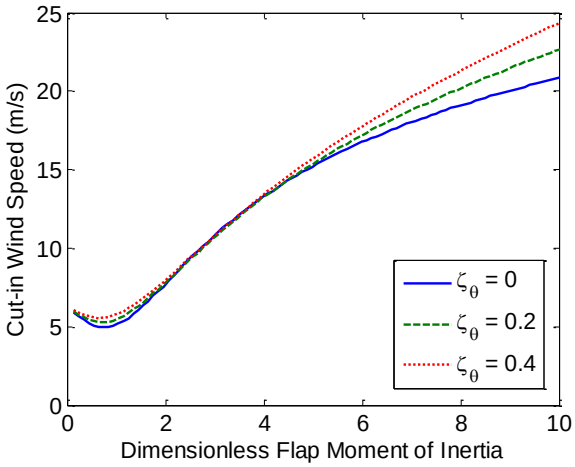

Figure 2.12 Change in cut-in wind speed as a function of flap mass moment of inertia.

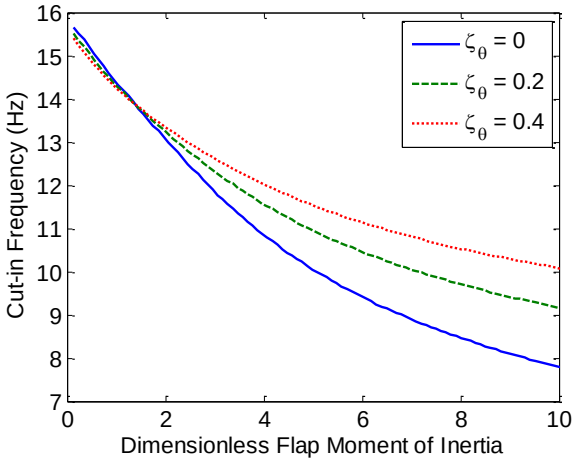

Figure 2.13 Change in cut-in frequency as a function of flap mass moment of inertia.

5.4. Sensitivity to Hinge Stiffness

While the flap moment of inertia changes the dependence between the wind speed and the flap natural frequency, the flap zero-wind-speed natural frequency can also be shifted by adding a torsion spring stiffness, K_θ, to the hinge axis. In the original aeroelastic energy harvester modeled and tested by Bryant and Garcia (2011), the hinge joint was allowed to rotate

freely with no mechanical spring stiffness. The aerodynamic forces acting on the flap were solely responsible for determining the natural frequency of the pitch degree of freedom at a given wind speed. Therefore with zero incident wind speed the pitch natural frequency was identically zero, indicating a rigid body mode of the system. Adding a torsion spring to this hinge joint creates a non-zero pitching natural frequency even in the absence of incident air flow and thereby changes the modal convergence characteristics of the system. The zero wind speed pitch natural frequency for this rotary mass-spring system is given by the standard lumped mass formula as

$$\omega_\theta = \sqrt{\frac{K_\theta}{I_P}} \tag{12}$$

where K_θ is the torsion spring stiffness and I_P is the mass moment of inertia of the flap about the hinge axis.

The effects of varying the hinge natural frequency parameter on the energy harvester cut-in conditions can be seen in Figures 2.14 and 2.15, where the hinge frequency is nondimensionalized by the first bending natural frequency of the beam. As shown by the figures, the cut-in wind speed curves show minimums within the range of hinge natural frequencies tested, while the frequency increases as the hinge natural frequency is increased throughout the range. With the zero-wind speed pitch natural frequency positioned closer to the heave natural frequency, lower aerodynamic forces are required to achieve the modal convergence, and the convergence point occurs at a higher frequency. Compared to the other parameters tested, however, the cut-in wind speed of the system shows much less sensitivity to this parameter, especially when damping is introduced in to the hinge joint.

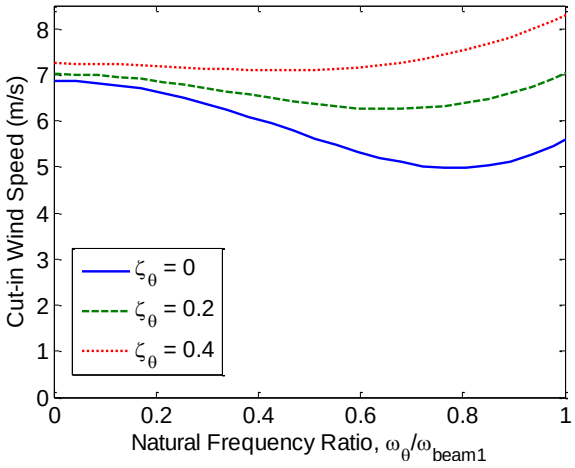

Figure 2.14 Change in cut-in wind speed as a function of hinge natural frequency.

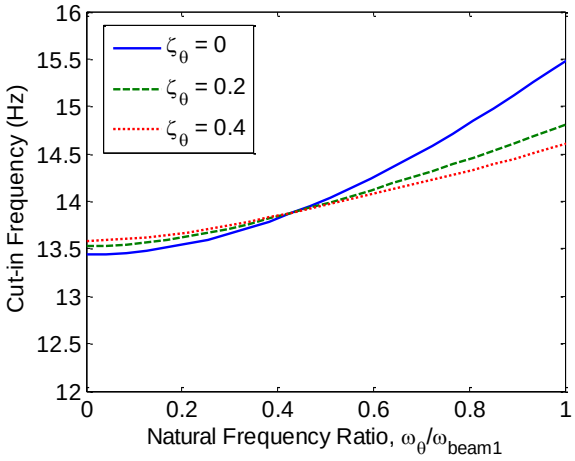

Figure 2.15 Change in cut-in frequency as a function of hinge natural frequency.

5.5 Sensitivity to Flap Chordwise Center of Mass Location

While the mass of the flap has already been shown to be an important parameter in the system, the distribution of that mass along the flap chord and the corresponding center of mass location of the flap also affect the aeroelastic instability. The chordwise center of mass location is given as the coordinate, e, which is non-dimensionalized as shown in Figure 2.1 such that $e = -1$ corresponds to the leading edge of the flap, $e = 0$ represents the mid-chord, and $e = 1$ is the

trailing edge. This parameter is found in the flap static unbalance term, x_θ, which is given by Eq. (1) and quantifies the amount of mechanical coupling between the heave and pitch degrees of freedom. The larger the separation between the flap center of mass and the flap hinge location, the larger in magnitude this static unbalance term becomes, and the more strongly coupled the pitching and heaving degrees of freedom become.

The cut-in wind speed and frequency show considerable variation with the center of mass location, as shown in Figures 2.16 and 2.17. The highest cut-in speeds occur when the center of mass approaches the hinge location (fixed at $a = -0.53$, or 0.235 chord), leading to low coupling between the heave and pitch modes of the system. Notably, flutter cannot occur in this system for values of $e < a$ as this would place the flap center of mass forward of the hinge, causing the heave-pitch coupling to oppose the growth of aeroelastic vibrations and act to stabilize the system regardless of wind speed. As the center of mass is shifted aft, a wide minimum in the cut-in wind speed occurs at approximately $e = -0.14$ or 0.43 chord. Moving the center of mass further aft beyond about $e = 0.18$ or 0.59 chord leads to a static divergence aeroelastic instability rather than flutter oscillations.

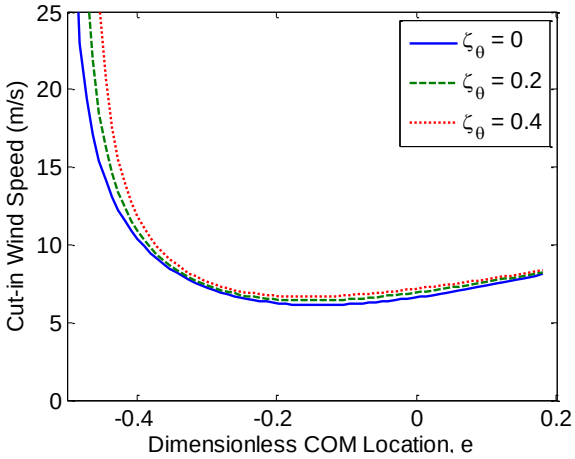

Figure 2.16 Change in cut-in wind speed as a function of flap center of mass location.

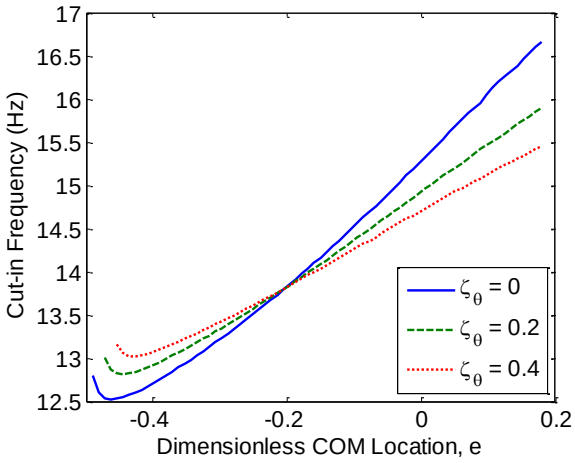

Figure 2.17 Change in cut-in frequency as a function of flap center of mass location.

5.6 Sensitivity to Flap Hinge Location

In addition to the mass and stiffness parameters of the system, the aeroelastic coupling characteristics are also involved in the system behavior. This aeroelastic coupling can be altered by changing the chordwise flap hinge joint position, which is expressed in the model variables as the nondimensional coordinate, a. This parameter is defined by the schematic shown in Figure 2.1 such that $a = -1$ corresponds to the leading edge of the flap, $a = 0$ represents the mid-chord, and $a = 1$ is the trailing edge. The linearized equations of motion show that the dimensionless hinge location affects the heave-pitch coupling because it appears in the flap static unbalance expression, x_θ, from Eq. (1). In addition, the parameter a appears on the right hand side of the flap torque balance given by Eq. (8) of the linearized model. Here, the parameter determines the aerodynamic torque generated by the lift force about the hinge axis by setting the distance between the aerodynamic center (assumed to be at the quarter-chord point) and the hinge. Finally, this parameter appears in both the lift force and pitching moment expressions of the unsteady aerodynamic model used to calculate the flap aerodynamic forces.

Figures 2.18 and 2.19 show the effects of varying this parameter on the cut-in wind speed and frequency of the system when hinge locations from the leading edge to the quarter-chord point are simulated. Downstream of the quarter-chord, the model predicts that flutter cannot occur, because the aerodynamic lift force now acts ahead of the hinge location, leading to static divergence of the flap rather than modal convergence flutter. The cut-in wind speed results for all cases of hinge damping ratio show the maximum cut-in wind speed occurs when the hinge is located at the leading edge ($a = -1$) and that a minimum occurs as the hinge location is varied. For the undamped hinge case, this minimum occurs at approximately $a = -0.64$ (0.18 chord) and 5.8 m/s, while increasing the hinge damping shifts the minimum point right and reduces the depth of the minimum. The frequency results show that the cut-in frequency decreases as the hinge point is moved aft throughout the range.

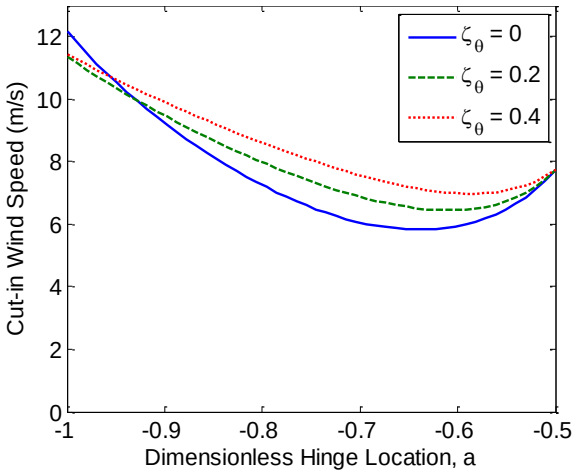

Figure 2.18 Change in cut-in wind speed as a function of flap hinge axis position.

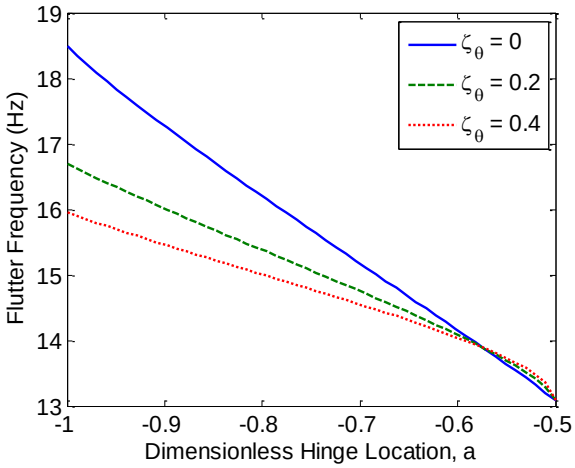

Figure 2.19 Change in cut-in frequency as a function of flap hinge axis position.

6. Implications of Parameter Sensitivity

Among the parameters tested, the non-rotating beam tip mass parameter shows the simplest effect on the cut-in characteristics. By adding tip mass, the heave natural frequency is reduced, leading to cut-in wind speeds and frequencies that vary approximately linearly with the first beam bending natural frequency. Despite the appealing simplicity of this approach, it is not without cost. Roundy et al. (Roundy, Wright, and Rabaey, 2003) showed that for a general vibration energy harvester being driven at its resonant frequency, the power output scales with resonant frequency cubed and vibration amplitude squared. Thus, a high bending natural frequency is desirable in the design of the energy harvester. A larger bending natural frequency increases the amount of power available while allowing for smaller amplitudes of motion, reducing the overall volume required and reducing the strain that must be endured by the system. Therefore, increasing the non-rotating tip mass might be best considered as a last resort to meet the cut-in wind speed requirements.

Although increasing the mass of the flap also alters the natural frequency of the piezoelectric beam by changing its total tip mass, the additional degree of freedom afforded by the hinge joint changes the effects on the cut-in results. Increasing flap mass produces several simultaneous effects, namely the reduced heave natural frequency, the additional pitch-heave coupling due to the added mass, and the additional inertia added to the heave degree of freedom. The result is that unlike continuously decreasing the cut-in wind speed as is possible by adding to the beam tip mass, increasing the flap mass produces a minimum in the cut-in wind speed curve, placing a bound on how far this parameter can reduce the cut-in wind speed. The useful range of this parameter is therefore limited in comparison to the beam fixed tip mass parameter. However, the minimum achievable cut-in wind speed occurs at a much higher beam natural frequency than would by possible by matching this cut-in wind speed by adjusting the fixed tip mass. This makes the flap mass parameter a more useful design tool than simply adding fixed tip mass to the beam, but, increasing this parameter still does suffer from an associated cost in the bending natural frequency. Increasing this parameter should likely be reserved, therefore, for cases where the desired cut-in speed cannot be achieved by means that do not reduce the bending natural frequency.

This study has shown that by adding a torsion spring stiffness to the pitch degree of freedom, the hinge natural frequency alone can also be modified to affect the cut-in characteristics of the system. However, this effect becomes minimal when practical levels of damping in the hinge are considered. As shown in Figure 2.14, the undamped ($\zeta_\theta = 0$) hinge simulation showed a reduction in cut-in wind speed of 28% compared to the freely rotating (zero natural frequency) hinge, but when the damping is increased to $\zeta_\theta = 0.4$ the curve showed a cut-in wind speed reduction of merely 2%. Therefore, unless the dissipative forces can be

maintained to very low levels, stiffening the hinge joint is unlikely to be a useful method of tuning the system cut-in wind speed. On the other hand, in applications that do not require large amplitudes of pitch motion, the relative insensitivity of this parameter may allow the bearings to be eliminated entirely in favor of a flexure joint that would be immune to mechanical wear and environmental fouling.

Moving the hinge location along the flap chord achieved moderate influence on changing the cut-in wind speed of the system, with the minimum wind speed location occurring slightly forward of the 1/4 chord point. Compared to placing the hinge at the flap leading edge, varying this parameter achieved reductions in cut-in wind speed of up to 54% with the undamped hinge or 41% with the hinge damping set to $\zeta_\theta = 0.4$. This change introduces no penalty in the natural frequency and no additional complexity to the design of the energy harvester and is therefore a reasonable design tool for decreasing the cut-in wind speed of the device.

Finally, the two parameters governing the chordwise mass distribution of the flap, the flap mass moment of inertia and the flap center of mass location, showed the greatest promise to act as design parameters for changing the cut-in wind speed of the energy harvester. The cut-in wind speed exhibited a significant sensitivity to these parameters and produced a minimum value in both cases. Varying these parameters has broad effects on the system dynamics, changing the aerodynamic pitch natural frequency and the pitch-heave coupling acting in the system, respectively, without requiring changes in the bending frequency of the piezoelectric beam or requiring additional mass or added system complexity. These parameters, therefore, should be the designer's first choice when tuning the energy harvester to meet the cut-in wind speed requirements of the intended application.

7. Experimental Verification

As a simple experimental verification of the model-predicted parameter sensitivity effects presented above, we consider the aeroelastic flutter energy harvester shown in Figure 2.2 equipped with a flap with a variable chordwise mass distribution. The model-predicted parameter variation curves reveal that the cut-in wind speed of the system shows considerable sensitivity to the distribution of mass along the flap chord, which is quantified by the flap center of mass location, e, and the flap mass moment of inertia about the hinge axis, I_P. While these parameters are treated independently in the above analysis so that the effect of each quantity can be explicitly studied, in the experimental apparatus they are altered simultaneously by moving a set of masses forward or aft along the chord of the flap, allowing the mass moment of inertia and center of mass position to be varied while all other beam and flap parameters are held fixed as listed in Tables 2.1 and 2.4 respectively. The cut-in wind speed and frequency of the system was measured in a low speed, open circuit wind tunnel with a 25×25×100 cm test section and a maximum wind speed of approximately 9.0 m/s. An Omega HHF42 probe hot wire anemometer was used to measure the flow speed, while the vibration frequency was measured directly from the beam's piezoelectric transducer output voltage using an Agilent DSO6014A digital oscilloscope.

Figure 2.20 plots the variation in the observed cut-in wind speed as a function of both the flap center of mass location and the mass moment of inertia for the experiment and the corresponding model predictions. The experimental and model-predicted results show similar trends and values, with the model prediction for $\zeta_\theta = 0.4$ showing the best agreement. The cut-in frequency results of Figure 2.21 show weaker, but still reasonable agreement, with the model

results shifted almost 2 Hz higher than the experiment and showing a more pronounced peak. The results of the experiment confirm that the model can not only reasonably predict the sensitivity and trend of the system cut-in conditions to changes design parameters, but that the flap mass distribution can be easily tuned in a practical energy harvester to produce a minimum cut-in wind speed for a given piezoelectric beam configuration and physical device size.

Table 2.4 Flap parameters for variable chordwise mass distribution experiment.

Parameter	*Symbol*	*Value*	*Units*
non-rotating tip mass	m_{NR}	6.4×10^{-3}	kg
flap mass	m_F	8.4×10^{-3}	kg
flap mass moment of inertia	I_P	0.017 to 0.10	kg·cm^2
flap hinge location	a	−0.53	unitless
flap center of mass location	e	0.39 to 0.50	unitless
flap hinge stiffness	K_θ	0	N·m/rad

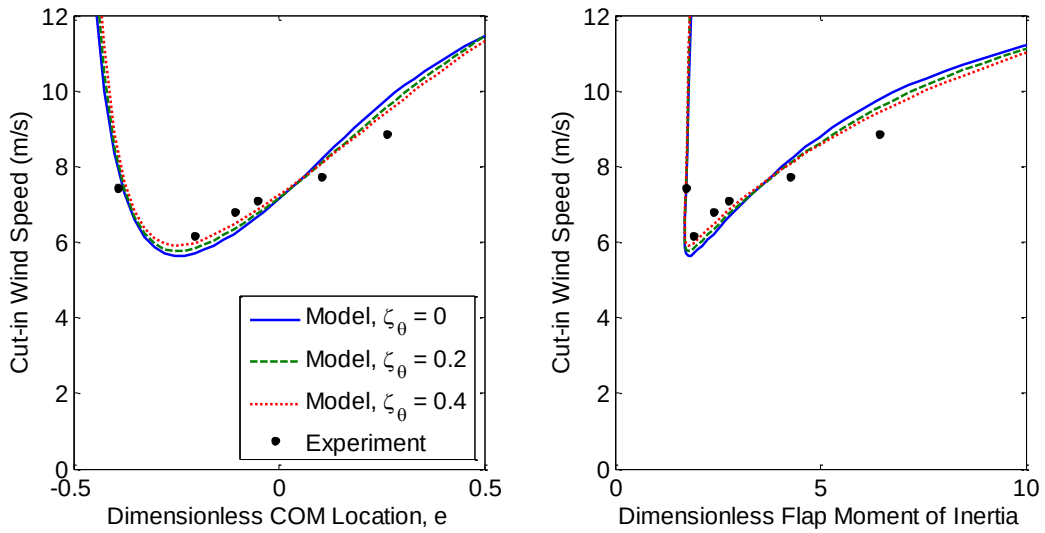

Figure 2.20 Experimental and predicted effects of varying flap mass distribution on the cut-in wind speed of the system.

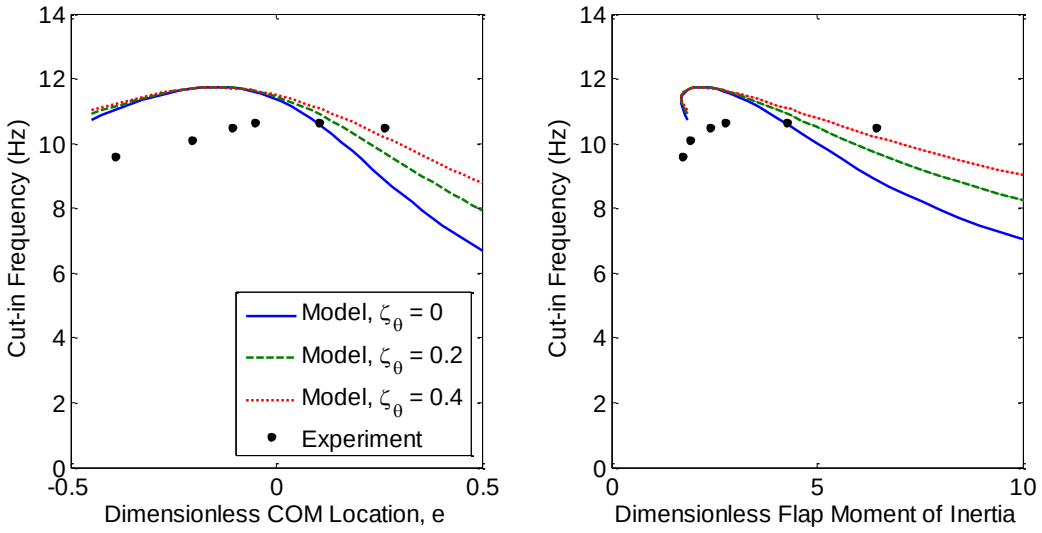

Figure 2.21 Experimental and predicted effects of varying flap mass distribution on the cut-in frequency of the system.

8. Conclusions

The problem of designing an aeroelastic flutter energy harvester for a given application requires matching the device parameters to the expected range of wind speeds and the power output requirements of the system. This study has examined the effects of several system design parameters on the minimum wind speed required to excite flutter vibrations and thereby generate power. Significant changes in the cut-in wind speed and frequency of the aeroelastic flutter energy harvester where shown to be achievable without altering the physical footprint or dimensions of the system and its components. Instead, the aeroelastic system behavior is tuned by modifying the component mass and stiffness parameters that govern coupling effects between the interacting degrees of freedom intrinsic to the modal convergence flutter instability. While all the parameters examined were shown to affect the cut-in wind speed of the system, there was a broad range in the strength of the sensitivity and the practical consequences of altering each system parameter. This chapter thus serves as a design guide to the tuning of flutter energy

harvesters to meet desired cut-in wind speed specifications. Of the parameters tested, the flap mass properties including the flap center of mass location, the flap mass moment of inertia, and the flap mass show the strongest effects on the cut-in wind speed of the system. Properly tuning these parameters can allow a high beam natural frequency to be maintained for maximum power density, while minimizing the wind speed required to initiate sustained flutter vibrations and begin harvesting energy form the wind.

In addition to the cut-in characteristics investigated here, the system parameters will also influence the steady state limit cycle motion of the energy harvester and thereby affect the power output of the device. While this investigation has established the relationships between the system parameters and the cut-in conditions, extending these relationships to the steady state operating regime over a range of flow speeds is a crucial next step in determining the optimal design of the flutter energy harvester for any intended application. Future work will address the dependence of the structural and aerodynamic nonlinearities responsible for the device limit cycle behavior and steady state power output on the system design parameters.

REFERENCES

Allen, J. J., and Smits. A. J., 2001, "Energy Harvesting Eel," Journal of Fluids and Structures, 15(3), pp. 629-40.

Andersen, A., Pesavento, U., and Wang, Z. J., 2005, "Unsteady Aerodynamics of Fluttering and Tumbling Plates," Journal of Fluid Mechanics, 541, pp. 65-90.

Anton, S. R., and Sodano, H. A., 2007, "A Review of Power Harvesting Using Piezoelectric Materials (2003-2006)," Smart Materials and Structures, 16, pp. R1-R21.

Bryant, M., and Garcia, E., 2011, "Modeling and Testing of a Novel Aeroelastic Flutter Energy Harvester," Journal of Vibrations and Acoustics, 133, 011010.

Dietl, J. M., and Garcia, E., 2010, "Beam Shape Optimization for Power Harvesting," Journal of Intelligent Material Systems and Structures, 21, pp. 633-46.

Dowell, E. H., Curtiss, Jr, H. C., Scanlan, R. H., Sisto, F., 1980, *A Modern Course in Aeroelasticity,* (Alphen aan den Rijn, The Netherlands: Sijthoff & Noordhoff).

Guyomar, D., Badel, A., Lefeuvre, E., and Richard, C., 2005, "Toward Energy Harvesting Using Active Materials and Conversion Improvement by Nonlinear Processing," IEEE Trans. on Ultrasonics, Ferroelectrics, and Frequency Control, 52, pp. 584-95.

Hagood, N. W., Chung, W. H., and von Flotow, A., 1990, "Modeling of Piezoelectric Actuator Dynamics for Active Structural Control," Journal of Intelligent Material Systems and Structures, 1, pp. 327-54

Hodges, D. H., and Pierce, G. A., 2002, *Introduction to Structural Dynamics and Aeroelasticity*, (Cambridge, UK: Cambridge University Press).

Khalak, A., and Williamson, C. H. K., 1999, "Motions, Forces, and Mode Transitions in Vortex-Induced Vibrations at Low Mass-Damping," Journal of Fluids and Structures, 13, pp. 813-51.

Kwon, S. D., 2010, "A T-shaped Piezoelectric Cantilever for Fluid Flow Energy Harvesting," Applied Physics Letters, 97, 164102.

Peters, D. A., Karunamoorthy, S., and Cao, W. M., 1995, "Finite State Induced Flow Models; Part I; Two Dimensional Thin Airfoil," Journal of Aircraft, 32, pp. 313-22.

Pobering, S. and Schwesinger, N., 2004, "A Novel Hydropower Harvesting Device," Proc. 2004 International Conference on MEMS, NANO and Smart Systems, pp. 480–85.

Robbins, W. P., Morris, D., Marusic, I., and Novak, T. O., 2008, "Wind-Generated Electricity Using Flexible Piezoelectric Materials," Proc. 17th IEEE International Symposium on the Applications of Ferroelectrics.

Roundy, S., Wright, P. K., and Rabaey, J., 2003, "A study of Low Level Vibrations as a Power Source for Wireless Sensor Nodes," Computer Communications, 26, pp. 1131-44.

Sodano, H. A., Park, G., and Inman, D. J., 2004, "Estimation of Electric Charge Output for Piezoelectric Energy Harvesting," Journal of Strain, 40, pp. 49-58.

Taylor, G. W., Burns, J. R., Kammann, S. M., Powers, W. B., and Welsh, T. R., 2001, "The Energy Harvesting Eel: A Small Subsurface Ocean/River Power Generator," IEEE Journal of Oceanic Engineering, 26, pp. 539-47.

van Oudheusden, B. W., 1996, "Rotational One-Degree-of-Freedom Galloping in the Presence of Viscous and Frictional Damping," Journal of Fluids and Structures, 10, pp. 673-89.

Wickenheiser, A. M. and Garcia, E., 2010, "Power Optimization of Vibration Energy Harvesters Utilizing Passive and Active Circuits," Journal of Intelligent Material Systems and Structures, 21, pp. 1343-61.

This chapter originally appeared as:

Bryant, M., and Garcia, E., 2011, "Aeroelastic Flutter Energy Harvester Design: The Sensitivity of the Driving Instability to System Parameters," Smart Materials and Structures, 20, 125017. Reprinted by permission of IOP Publishing Ltd.

CHAPTER 3
WAKE SYNERGIES ENHANCE PERFORMANCE IN AEROELASTIC VIBRATION ENERGY HARVESTING

1. Abstract

This chapter experimentally demonstrates that a closely spaced array of aeroelastic flutter energy harvesters can exploit synergistic wake interactions to outperform the same number of harvesters operating in isolation. The fluttering motion of each energy harvester imparts an oscillating vortex wake into the flow downstream of the device. Wind tunnel experiments with arrays of two and four flutter energy harvesters show that this wake structure has significant effects on the vibration amplitude, frequency, and power output of the trailing devices. These wake interaction effects are shown to vary with the stream-wise and cross-stream separation distance between the harvesters. Over a defined range of separations, an advantageous frequency lock-in between the devices arises. When this occurs, the trailing harvesters can extract additional energy from the wake of upstream harvesters, causing larger oscillation amplitudes and higher power output in the trailing devices. Experiments to characterize this variation in power output due to these wake interaction effects and to determine the optimal spacing of the energy harvesters are presented and discussed. Smoke-wire flow visualization is used to examine the wake structure and investigate the mechanism of the array interactions.

2. Introduction

Both nature and engineering offer myriad examples of interactions between flexible structures and fluid flows ranging in scale from wind loading of thousand meter long suspension

bridges to microorganism locomotion. Traditionally, engineers have primarily studied problems of isolated elastic structures interacting with free stream flows, such as the classical wing flutter problem (Theodorsen, 1934). Recently, however, both the engineering and biological communities have produced an increasing number of studies into the more complex interactions that can occur when deformable structures interact with the vortex wakes of upstream bodies. Several publications have addressed the mechanics of fish swimming in the wake of an upstream bluff body that periodically sheds vortices in a von Kármán vortex street. One such study found that live trout alter their swimming kinematics and adopt a "Kármán gait" that is characterized by large body deflections and curvatures with a swimming frequency that matches the vortex shedding frequency of the upstream bluff body (Liao, Beal, and Lauder, 2003). A subsequent study found that even a dead trout can swim upstream by extracting energy from the wake of an upstream cylinder and generating thrust-producing body deflections (Beal et al., 2006), while an earlier study showed whale flukes are capable of absorbing energy from surface waves and creating thrust whether the whale is alive or dead (Bose and Lien, 1990).

Recent works have also investigated the interactions between pairs and groups of deformable bodies passively flapping in flowing fluids. These studies have uncovered multi-body flow interactions that are potentially advantageous for arrays of aeroelastic vibration energy harvesting devices. Experimental investigations of tandem flag-like flexible bodies have shown that for certain spatial configurations the trailing body can extract additional energy from the wake of the leader, developing an "inverted drafting" phenomena with larger amplitudes of motion and increased drag force for the trailing body. The motion of the upstream body, however, is largely unchanged from the case of a lone body. This result has been demonstrated in soap film flows using flapping thread filaments for the case where the filament leading edges

are rigidly fixed in the flow (Ristroph and Zhang, 2008) as well as when the downstream filament is free to translate in the cross-stream direction but restrained in the flow direction (Jia and Yin, 2008). For these filament structures, the Reynolds numbers based on body length was 10^4 (Ristroph and Zhang, 2008) and 1400 to 3500 (Jia and Yin, 2008), respectively. Numerical investigations of the multibody flapping interaction problem have also predicted similar results for tandem flapping flags using inviscid simulations (Alben, 2009) as well as viscous cases (Zhu, 2009: Kim, Huang, Sung, 2010). When the Reynolds number is set so low that flapping no longer occurs in the flags, the traditional drafting situation as in rigid bodies reemerges (Zhu, 2009).

Exploiting this inverted drafting phenomenon with novel flow energy harvesting methods may allow increased performance in arrays of fluid flow energy harvesting devices. Conventional horizontal axis wind turbines experience detrimental wake interference as far as 20 rotor diameters downstream of a leading turbine, producing reductions in energy output and aerodynamic array efficiencies that are always less than unity (Hau, 2006). In practice, this energy reduction ranges from 2 to 20%, depending on spacing, wind direction, and ambient turbulence, and results from both decreased incident wind speed and larger turbulence intensity in the wake (Jain, 2011). Contrary to traditional wind power conventions, our study experimentally demonstrates that the inverted drafting phenomenon can be used to enhance performance in arrays of aeroelastic flutter energy harvesters by increasing the power output of the trailing devices. We show that this effect exists in arrays of both two and four flutter energy harvesters. The flutter energy harvester under consideration here is based on the device proposed and modeled by Bryant and Garcia (2011) and utilizes a cantilevered piezoelectric beam with a flat plate flap connected to the free end of the beam by a hinge joint. The flap is

thus afforded two degrees of freedom; pitching due to rotation about the hinge joint, and heaving due to deflections of the beam tip. Above a critical flow speed this device is subject to a modal convergence flutter instability (Theodorsen, 1934; Dowell, et al., 1980; Hodges and Pierce, 2002) and experiences stable limit cycle oscillations over a range of wind speeds (Bryant and Garcia, 2011).

3. Apparatus and Methods

3.1. Aeroelastic Flutter Energy Harvester

The flutter energy harvester design used in the present study is shown in Figure 3.1, and is based on the prototype device previously described by Bryant and Garcia (2011). The substrate of the piezoelectric beam consists of a spring tempered 301 stainless steel beam with a thickness of 0.381 mm and a width of 25mm. The electromechanical transduction is provided by pair of Mide QP-10N piezoelectric patches laminated to the root of the beam in a bimorph configuration. At the free end of the beam, a plastic clasp houses a pair of ball bearings and a carbon fiber shaft to create a low-friction hinge joint to the flap. A simple flat plate with chord 5.9 cm, span 13.6 cm, and a thickness of 1.5mm is used as the flap. The fixed end of the beam is secured by a streamlined clamp and held in the flow by a rigid sting that is secured to the floor of the wind tunnel. The total body length of each harvester is approximately 36 cm in the stream-wise direction. Previous experiments showed that the flutter stability boundary for this device occurs at wind speeds of about 2 m/s. While this design is in no way claimed to be optimal, it provides a useful test platform for investigating aerodynamic interaction effects in arrays of passively fluttering energy harvesters.

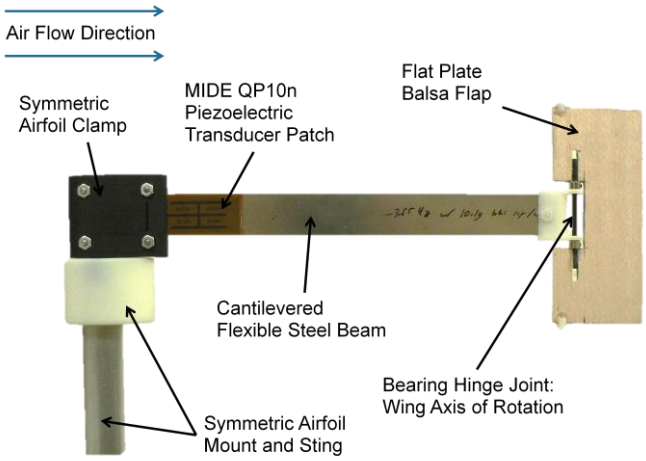

Figure 3.1 Photograph of the aeroelastic flutter energy harvesting experiment with major components labeled.

3.2. Experimental Equipment

Wind tunnel experiments were conducted in an open circuit, suction type wind tunnel with a test section that is 1.2 m wide × 1.35 m tall × 3.2 m long and has turbulence intensity up to 2%. Six axial fans at the tunnel outlet control the airflow in the test section, while a pitot-static tube and an Omega HHF42 probe hotwire anemometer were used to monitor the wind tunnel flow velocity. The flutter energy harvesters are positioned at the mid-height of the wind tunnel by streamlined aluminum stings. Figure 3.2(a) shows a photograph of two flutter energy harvesters in the wind tunnel test section.

In order to create a simple method to measure changes in the output power of each device, each energy harvester is connected to an independent resistive load that is tuned for maximum power transfer. The voltages across the load resistors are monitored using an Agilent 54622A oscilloscope and recorded using a National Instruments data acquisition system. The data acquisition is performed using LabVIEW software running on a PXI-8176 controller and

PXI-6052E I/O card with a BNC-2120 breakout board to interface with the energy harvesters. The piezoelectric voltages across the resistive loads were on the order of ±30 V, while the data acquisition system has a maximum range of ±10 V. In order to step down the voltage levels to within the limits of the data acquisition system and to ensure that the currents from the energy harvesters pass through the proper matched loads, voltage dividers are incorporated into the resistive loads and simple unity gain buffers using UA741 op-amps were utilized. The op-amps act as voltage buffers to ensure that the total effective impedance seen by each piezoelectric harvester is equal to the matched load and is unaffected by the data acquisition system.

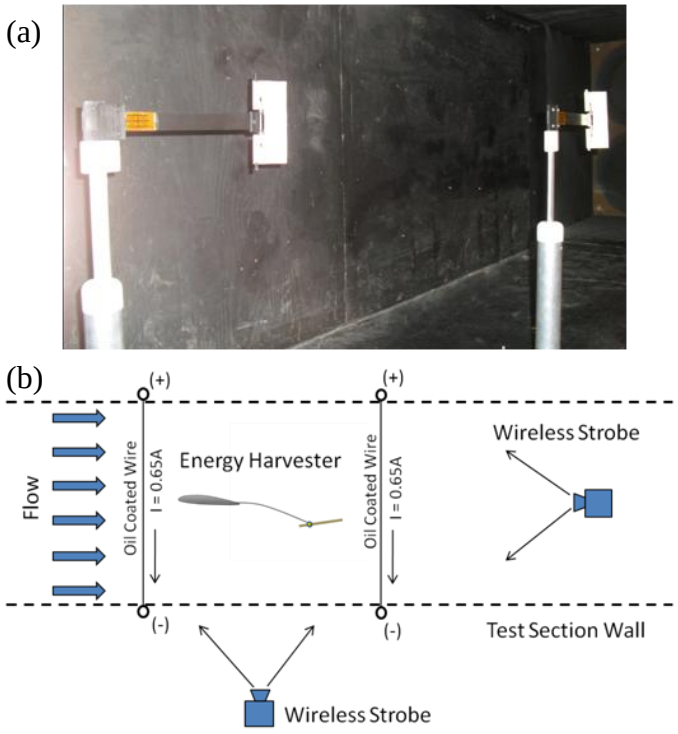

Figure 3.2 (a) Two aeroelastic flutter energy harvesters mounted in the wind tunnel test section in tandem configuration. (b) Overhead schematic view of the smoke wire flow visualization setup used to image the wake of the flutter energy harvesters. The camera is mounted above the wind tunnel test section and is remotely operated by a tethered laptop computer.

In addition to the measurements of the energy harvester outputs made using the data acquisition system, qualitative insight into the wake interactions occurring in the flutter energy

harvester array can be garnered using wind tunnel flow visualization techniques. In particular, we implemented a smoke wire flow visualization system similar to that described by Yarusevych et al. (2009). As diagramed in Figure 3.2(b), the apparatus uses ohmically heated Ni-Cr wires to generate a sheet of smoke by vaporizing a coating of high viscosity mineral oil. The wire diameter was sized to minimize the addition of turbulence to the flow (Yarusevych, Sullivan, Kawall, 2009), and the wire length spanned the wind tunnel cross section. Images were captured by a Nikon D300 digital still camera with a 35mm f/1.4 lens, while lighting was provided by a pair of strobe lights (Nikon SB-800 and Sigma EF-610) wirelessly slaved to the camera shutter. Custom attachments were fitted to the strobe units to focus the light output onto a thin, wide light sheet capable of illuminating the smoke sheet with minimal scatter to the background. As suggested by Yarusevych et al. (2009), the primary light source is placed in the wind tunnel downstream of the subject. The secondary strobe is placed outside the test section and illuminates the flutter energy harvester from the side to eliminate shadows created by the deforming body.

3.3. Experimental Procedure

In order to assess the effects of the relative spatial configuration of the devices in the array, the positions of the downstream energy harvesters were varied within the wind tunnel test section while the position of the leader was fixed. Experiments varied both the stream-wise separation distance, X, and the cross-stream separation distance, Y, as defined in Figure 3.3. For each configuration tested, the behavior of each energy harvester was first measured independently before the harvesters were operated in tandem. The individual harvester tests were conducted at the same locations in the wind tunnel as were used in the tandem experiments

to ensure that no spurious effects due to the wind tunnel flow characteristics were being introduced. All tests were performed at 8.1 m/s wind speed with a Reynolds number of 190,000 based on the overall body length of a single energy harvester. This corresponds to the wind speed at which previous experiments showed the maximum power output for these energy harvesters (Bryant and Garcia, 2011).

Wire leads attached to the electrodes of the piezoelectric patches extended outside the wind tunnel test section to the loads, buffering circuits, and data acquisition system. Before the power output could be measured, an appropriate resistive load was set for each trial to provide the resistance for maximum power transfer through the electromechanical system. Guyomar et al. (2005) provide the optimal resistive load for maximal power transfer from a weakly coupled piezoelectric energy harvester as

$$R_{opt} = \frac{1}{C_P \omega} \tag{1}$$

where C_P is the capacitance of the piezoelectric beam and ω is the frequency of vibration. The capacitance of the harvester's piezoelectric transducers was measured using a multimeter, and the flutter limit cycle oscillation (LCO) frequency was measured using the oscilloscope.

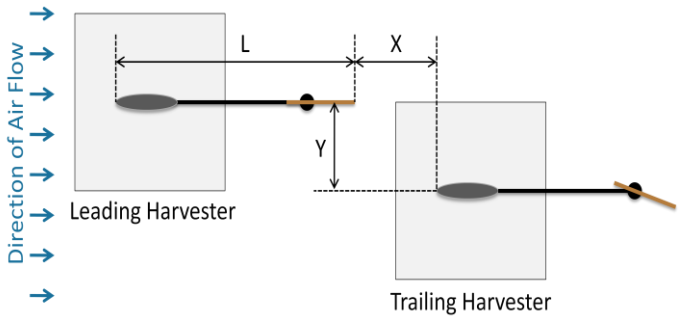

Figure 3.3 Overhead view of the two-harvester experiment with coordinates defined.

Previous tests indicated that the flutter LCO frequency of an isolated energy harvester is a function only of the ambient dynamic pressure. Since the wind speed and fluid density were kept constant in this study, the flutter LCO frequency of a harvester independently placed in the wind tunnel was expected to be constant, but the flutter frequency behavior when multiple harvesters were operating together was found to change depending on the array configuration. The frequency was therefore monitored during all trials and the resistive load was always tuned to the optimal value whether the harvesters were operating alone or together in the wind tunnel. Once the appropriate resistive load was determined for each energy harvester, the steady state AC voltage across the resistor was recorded using the National Instruments data acquisition system and LabView. The software recorded the voltage signal for 60 seconds at 1000Hz, and stored voltage versus time data for each trial. Considering that the energy harvester oscillation frequency was approximately 5Hz, the 1000Hz sample rate was more than adequate to avoid aliasing in the data.

For each X,Y spacing between harvesters, first the leading harvester was placed alone in the tunnel, its optimum load impedance was determined, and its corresponding (60-second) steady state voltage signal across the resistive load was stored using the data acquisition system. The leading harvester was then removed and this process was repeated for each of the trailing harvesters alone in the test section, placed a distance X downstream and Y cross-stream away from location where the previous harvester was placed. Finally, the same process was repeated for all the harvesters operating simultaneously in the tunnel in the X,Y configuration specified for the trial.

In order to give the stream-wise and cross-stream separation distances a relative scale for this system, the distances are nondimensionalized by the total body length, L, of each energy

harvester. It was hypothesized that the wake of the leading harvester would affect the trailing harvester up to some distance X/L behind it, after which the wake effects should dissipate and become insignificant. Based on the available wind tunnel test section length, trials were conducted from X/L = 0, up to X/L = 6, or six harvester lengths separating the two devices in the stream-wise direction, in increments of $\Delta X/L = 0.5$. It was also hypothesized that the leading harvester's wake would have different effects on the trailing harvester at different cross-stream separations, and therefore a range of cross-stream separations between harvesters was also to be tested. Due to the limited width of the wind tunnel test section, and in order not to have the harvesters enter the sidewall's boundary layer, tests were conducted for Y/L = 0, 0.5 and 1. As a result, the combination of all the test locations forms a rectangular grid of locations behind the trailing edge of the leading harvester at which the trailing harvester's behavior was investigated. Because of the harvesters' symmetric oscillations, trials were only made to one cross-stream side of the leading harvester. That is, it was assumed that for a given streamwise separation, the behavior of the trailing harvester at Y/L = 0.5 would be identical to its behavior at Y/L = −0.5, therefore the trailing harvester was offset to only one side of the leading harvester, and symmetric behavior is assumed for the other side.

3.4. Data Processing and Analysis

While an isolated flutter energy harvester operating at steady flow conditions produces a sinusoidal voltage with approximately constant amplitude and therefore the same average output power over every oscillation cycle, wake interactions between multiple energy harvesters can produce more complex effects. Therefore, a method to quantify the variation in power output by the energy harvester due to time-varying vibration amplitudes was required. This was

accomplished in a MATLAB data processing script. The AC voltage data was parsed into half-cycle segments using a zero crossing detection scheme. With 60 seconds of data recorded for each test and a harvester vibration frequency of nearly 5 Hz, each test yields approximately 600 of these half-cycle segments. For each half-cycle segment, the RMS voltage value was determined according to the formula

$$V_{rms,i} = \sqrt{\frac{1}{t_{1,i} - t_{0,i}} \int_{t_{0,i}}^{t_{1,i}} V^2 dt} \tag{2}$$

where $t_{0,i}$ and $t_{1,i}$ are the starting and ending times of the i^{th} half-cycle. The half-cycle average power through the load can then be calculated as

$$P_{avg,i} = \frac{\left(V_{rms,i}\right)^2}{R_{opt}} \tag{3}$$

where R_{opt} is the matched load resistance. The overall average power through the load for the entire trial can then be calculated as the mean of the half-cycle averages or

$$P_{AVG} = \frac{1}{C} \sum_{i=1}^{C} P_{avg,i} \tag{4}$$

where C is the number of half cycles included in the data set. Next, the variation in the half-cycle average powers can then be quantified by calculating the standard deviation according to

$$\sigma = \sqrt{\frac{1}{C} \sum_{i=1}^{C} \left(P_{avg,i} - P_{AVG}\right)^2} \tag{5}$$

For the simple case of a constant amplitude sinusoidal voltage history, the half-cycle average power of Eq. (3) and overall trial average power of Eq. (4) are identical, so that the standard deviation vanishes and this computation collapses to the familiar RMS power of an AC signal.

In order to facilitate comparison of the power and flapping frequency of each device as the separation is varied, the power and frequency measurements must be appropriately normalized. This accounts for slight differences in the construction and parameters of the devices. The average power of each device when operating in tandem is therefore normalized by the corresponding values of average power when that harvester is tested alone in the same position. The normalized power of each harvester for a given spatial configuration (X,Y) is expressed by

$$\overline{P}_{AVG} = \frac{P_{AVG,TANDEM}}{P_{AVG,ALONE}} \tag{6}$$

where the subscripts *TANDEM* and *ALONE* denotes a test with both energy harvesters operating in the wind tunnel simultaneosuly, or just one operating in isolation, respectively. These equations are applied to each energy harvester in the array for every (X,Y) configuration tested. Finally, the aerodynamic array efficiency often used to describe large scale wind power installations offers a direct measure of the effects of the harvester wake interactions on the overall performance of the system (Hau, 2006). This dimensionless ratio compares the total power output of the harvesters when operating simultaneously in the array to the total power output when the same harvesters operate in isolation, or

$$\eta_{ARRAY} = \frac{\sum_{k=1}^{N} P_{k,AVG,TANDEM}}{\sum_{k=1}^{N} P_{k,AVG,ALONE}} \tag{7}$$

where N is the total number of energy harvesters in the array, and k designates the particular harvester under consideration in the array.

4. Results and Discussion

4.1. Array of Two Energy Harvesters

In order to determine the aerodynamic interaction effects of the two aeroelastic flutter energy harvesters in tandem, it is first necessary to understand the baseline behavior of each energy harvester when operating in isolation. Table 3.1 summarizes the average power and frequency characteristics for each energy harvester when tested alone in the wind tunnel. While the two devices were built to the same specifications, measurable differences are observed in their steady state power output and flutter LCO frequency, with Harvester 2 showing a slightly higher frequency and lower power output than Harvester 1. In the two harvester array experiments described below, Harvester 1 is placed in the leading position, while Harvester 2 is placed in the trailing position.

Table 3.1 Comparison of the behavior of the two energy harvesters when operating alone with Re = 190,000.

Parameter	*Harvester 1*	*Harvester 2*
Steady State Power Output	1.49 mW	1.38 mW
Flutter LCO Frequency	4.82 Hz	4.91 Hz

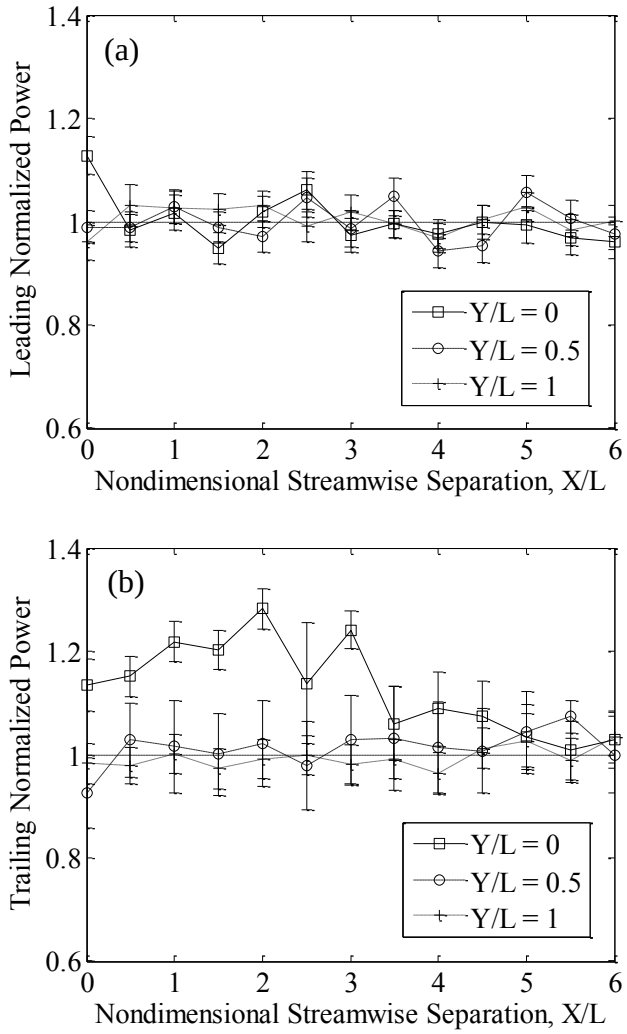

Figure 3.4 Variation in normalized power output as a function of separation distance in a tandem two harvester array for (a), the leading energy harvester, and (b), the trailing energy harvester. Error bars represent ± one standard deviation from the mean over 60 seconds of data.

Figure 3.4(a) plots the normalized power output of the leading energy harvester as a function of the stream-wise separation distance for each of the three cross-stream separations tested. The normalized power output shows only minor fluctuation throughout the entire range of spatial configurations tested, and shows relatively small standard deviations indicating a nearly uniform amplitude in the output voltage waveform. The fact that the normalized output power is similar in magnitude for all separations tested indicates low sensitivity to the spatial configuration for

the leading harvester. In fact, the normalized power is approximately unity for the configurations tested, indicating that the presence of the trailing harvester does not strongly affect the behavior of an upstream device. The most notable exception to these observations is the point $X/L = 0$, $Y/L = 0$ where there is an approximately 15% increase in the power of the leading device when in tandem compared to when in isolation. This is the configuration of minimal separation between the devices, and may create an additional interaction effect between the flap of the leading device and the flow around the leading edge of the trailing harvester.

In contrast to the results for the leading harvester, the trailing harvester normalized power, as shown in Figure 3.4(b), shows significant interaction effects due to the tandem configuration. The case of zero cross-stream separation, where the trailing device is directly downstream of the leader, shows the most pronounced variation in normalized power output with separation distance. For all separations up to $X/L = 3.5$ the trailing harvester produces significantly more power when located downstream of the leading device than when it is in isolation, indicating synergistic wake interactions. The maximum occurs at two body lengths downstream, where the trailing device produces almost 30% more power when in tandem with the leader than when alone. The standard deviations in the power remain relatively low at the maximum power points, indicating nearly constant amplitude voltage outputs from the trailing energy harvester in these cases. For the trailing harvester located at $X/L = 2.5$, just downstream of the maximum power position, the power output locally drops and shows a much greater standard deviation than surrounding points along the $Y/L = 0$ curve. Downstream of $X/L = 3$, the trailing harvester power again returns to approximately the same magnitude as for an isolated harvester, suggesting the wake effects of the leader have dissipated.

The other cross-stream separations tested, *Y/L = 0.5* and *Y/L = 1*, do not show the synergistic power enhancement that was present when the energy harvesters were aligned in the stream-wise direction. Instead, the average power produced is always approximately unchanged from the isolated harvester case. However, another interesting trend is revealed. For *Y/L = 0.5*, the standard deviations are relatively large throughout the range, while for *Y/L = 1* they become much smaller. This likely indicates that when the cross-stream separation is increased to one body length, the trailing device is no longer being significantly influenced by the wake of the upstream harvester, regardless of the spacing in the stream-wise direction.

The aerodynamic array efficiency of Eq. (7) can be used to summarize the effects of the array spacing on the overall system power output, as shown by Figure 3.5. The efficiency of the array peaks at over 115% at the X/L = 2, Y/L = 0 configuration, with a slightly smaller peak of over 113% at X/L = 0, Y/L = 0. This not only confirms that wake synergies allow an array of harvesters to outperform the same number of isolated harvesters, but also shows that little separation is necessary between the two harvesters to take advantage of these benefits. Indeed, given that the average aerodynamic efficiency of the two harvesters with zero separation distance is within one standard deviation of the overall maximum efficiency, the zero separation configuration is likely to be the preferred design in many applications with limited available space.

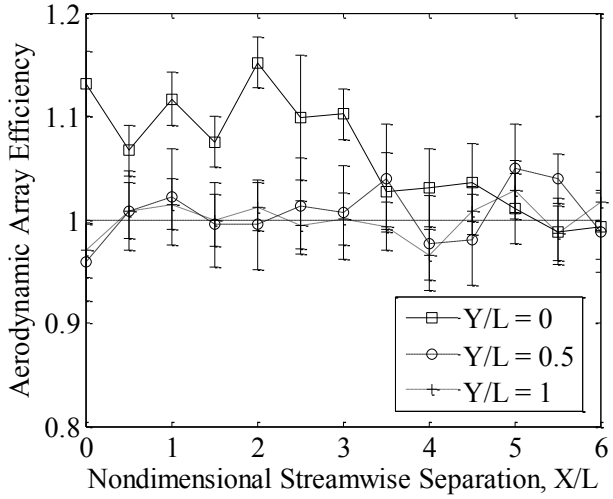

Figure 3.5 Aerodynamic array efficiency of the two tandem energy harvesters as a function of separation distance. Error bars represent ± one standard deviation from the mean over 60 seconds of data.

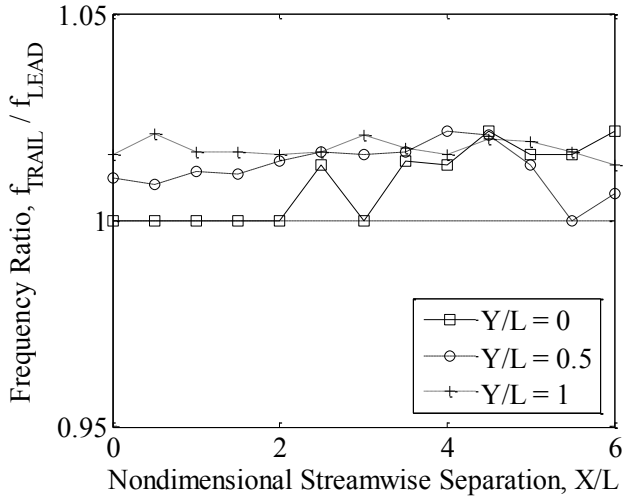

Figure 3.6 Comparison of leading and trailing harvester flutter frequencies as a function of separation distance.

Examining the flutter frequency data of the tandem harvester system shown in Figure 3.6 can shed additional light on the interactions that are occurring in this system. While Table 3.1 shows that when operating alone the energy harvesters flutter at different frequencies (4.82 Hz and 4.91 Hz for the leading and trailing harvesters, respectively), when operating in tandem the

flutter frequencies lock to a common value for certain configurations. For zero cross-stream separation, the frequencies of the two devices are effectively identical for $0 \leq X/L \leq 2$ and $X/L = 3$, the same positions where substantial synergistic enhancements occur in the trailing harvester power. These locations also correspond to low standard deviations in the output power due to changes in the voltage amplitude. The frequency lock also occurs for the test at $X/L = 5.5$, $Y/L = 0.5$. This separation corresponds to the maximum power and minimum deviation point for the trailing harvester $Y/L = 0.5$ curve, pointing to another, weaker synergistic interaction configuration. Much like the power data, the frequency comparison for the cross-stream separation of $Y/L = 1$ shows little change due to wake interactions or sensitivity to separation distance.

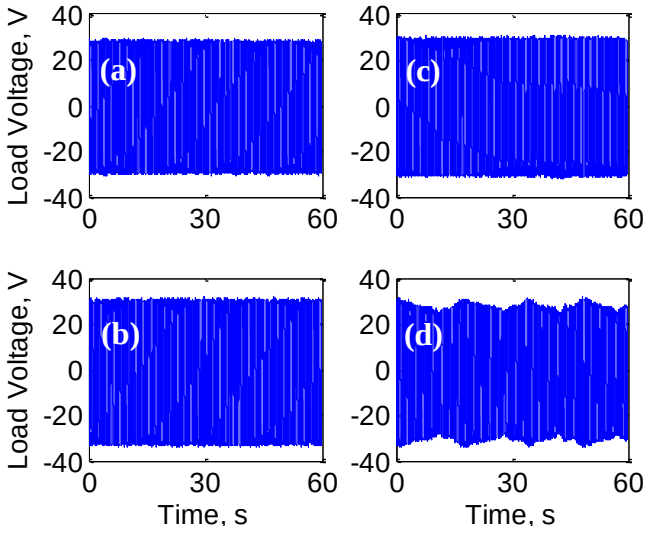

Figure 3.7 Output voltage histories for (a), leading harvester, X/L = 2, Y/L = 0, (b), trailing harvester, X/L = 2, Y/L = 0, (c), leading harvester X/L = 2.5, Y/L = 0, and (d), trailing harvester, X/L = 2.5, Y/L = 0.

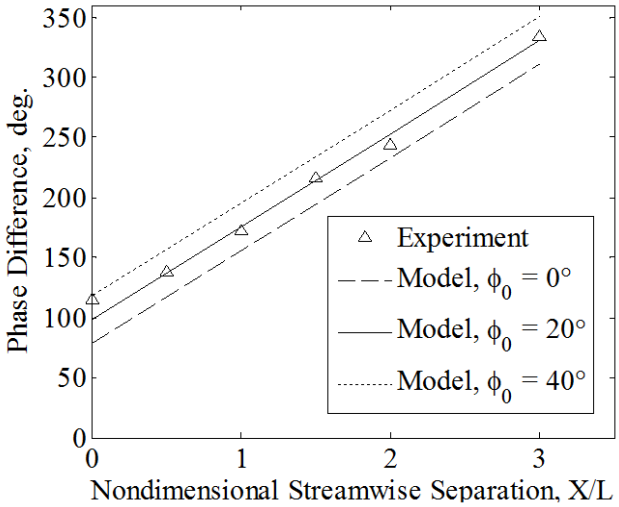

Figure 3.8 Phase difference of output voltages as a function of stream-wise separation distance for cases where frequency lock occurred with Y/L = 0.

The voltage waveforms from the leading and trailing energy harvesters change substantially depending on the flutter frequencies of the two harvesters. Figure 3.7 compares the leading and trailing energy harvester voltage histories for a typical configuration where the flutter frequencies are locked to the same value (X/L = 2, Y/L = 0) and where they are different (X/L = 2.5, Y/L = 0). The frequency locked case shows that both harvesters produce sinusoidal voltage waveforms with nearly steady amplitude, and with a larger amplitude for the trailing energy harvester. For the configuration with the flutter frequency mismatch, however, the trailing harvester voltage displays a changing amplitude in the form of a beat phenomenon. This beating results from the constantly changing phase between the devices, causing alternating instances of constructive and destructive interference. In both cases, the amplitude of the leading harvester output remains steady. For the cases where the flutter frequencies lock we observe an approximately linear relationship between the voltage phase difference and the stream-wise separation distance, as shown in Figure 3.8. This suggests that the elapsed time required for a wake feature from the leading energy harvester to travel downstream and reach the trailing

harvester is largely responsible for determining the phase difference between the motions of the energy harvesters. A simple model of this phase-spacing relationship is proposed in the next section.

4.2. Smoke Wire Flow Visualization Images

The smoke wire flow visualization shown in Figure 3.9(a) reveals that the wake of an isolated flutter energy harvester is composed of wake features at two distinct scales, a large scale wake structure and smaller vortex elements that exist within the gross wake. The large scale wake structure consists of a sinusoid that oscillates in the cross-stream direction following the motion of the energy harvester trailing edge and propagates downstream with the flow. Approximately one-half wavelength of this large scale wake structure is visible in Figure 9(a). As the large sinusoidal wake structure propagates downstream, its amplitude expands. This wake structure is a region of highly turbulent air composed of smaller eddies or vortices that are shed from both the leading and trailing edges of the flap as a result of the large angle of attack and stalled flow passing over the flap. These structures are sketched qualitatively over a full oscillation cycle in Figure 9(b). Figure 3.10 shows the flow past the trailing harvester for a two harvester array with a uniform flapping frequency at four different instants in the flapping cycle. The wake structure from the upstream harvester is visible as a curve of highly turbulent air stretching across each frame. The images show that the trailing harvester flap and the local wake structure of the leader oscillate across the stream with a small, approximately constant phase difference. Furthermore, the orientation angle of the flap appears to approximately match the local slope of the wake structure at all times in the flapping cycle. These observations are consistent with the linear relationship between phase difference and separation distance shown in

Figure 3.8; we have shown that the trailing harvester tip deflection maintains a small phase difference with the incident local wake, and clearly the time duration for any wake feature shed by the upstream harvester to travel downstream to the trailing harvester will vary linearly with the separation distance. With these observations in hand, we propose an equation to model the phase difference between the two frequency-locked energy harvesters according to

$$\phi = 360° \frac{f}{U_\infty}(X + L) + \phi_0 \tag{8}$$

where f is the flutter frequency, $(X+L)$ is the total distance between the trailing edges (or any reference feature) of the two harvesters, and ϕ_0 is the constant phase offset between the trailing harvester and the incident local wake. This formulation assumes that the wake of the leading harvester propagates downstream at the free stream flow velocity, U_∞. The results of this model are plotted in Figure 3.8 for several values of ϕ_0.

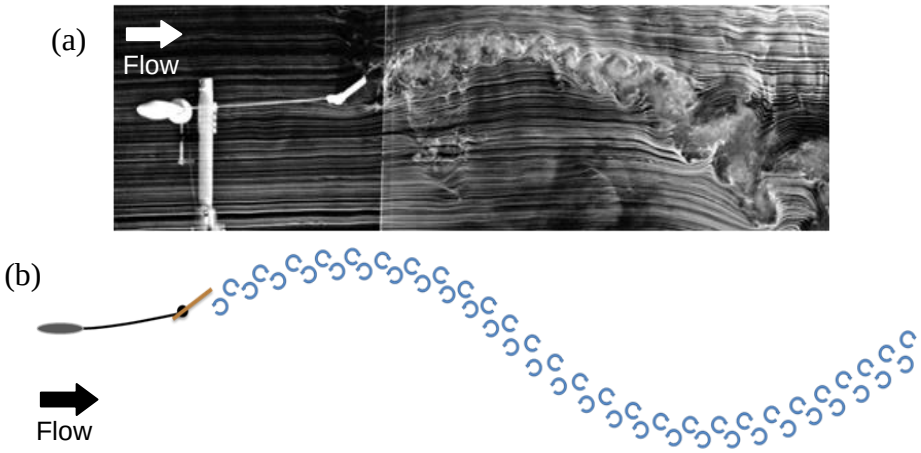

Figure 3.9. (a) Smoke wire flow visualization image of airflow over the fluttering energy harvester at U = 8.1 m/s and Re = 190,000. Smoke wires are placed both upstream and downstream of the energy harvester to enhance wake visibility. Camera exposure time was 1/5000 s with a focal ratio of f/1.4. (b) Conceptual sketch of the energy harvester wake structure with one full cycle of oscillation sketched.

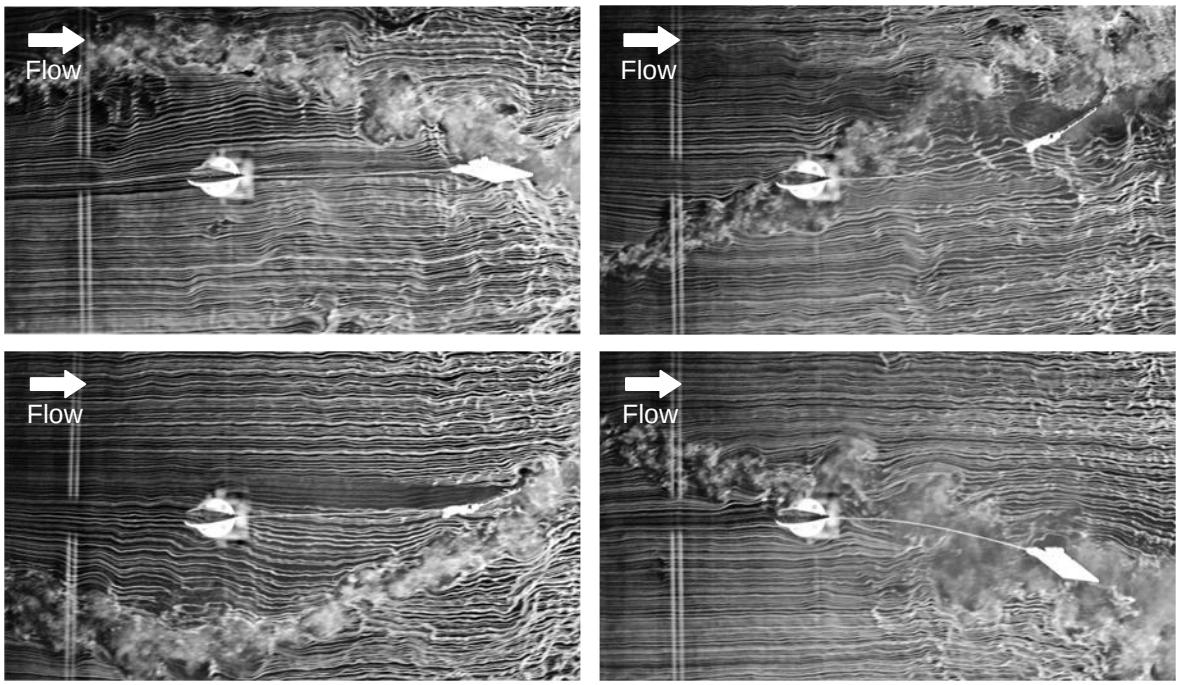

Figure 3.10 Smoke wire flow visualization images of airflow past the trailing energy harvester in a two-harvester array with U = 8.1 m/s and Re = 190,000. Four instances in the flapping cycle are shown. The leading harvester is positioned upstream with stream-wise separation distance X/L = 1.5 and cross-stream separation distance Y/L = 0. The leading and trailing harvesters flutter with the same frequency. Camera exposure time was 1/5000 s with a focal ratio of f/1.4.

4.3 Array of Four Energy Harvesters

After studying the interactions of a pair of energy harvesters, we expanded the array to a group of four harvesters. The two harvesters exhibited beneficial wake interactions with Y/L = 0 and a range of stream-wise separations, so the four harvester tests were conducted with Y/L = 0 and stream-wise separations up to the maximum feasible in the wind tunnel test section, X/L = 1.5. The four harvester arrangement is shown schematically in Figure 3.11. The same wind speed, experimental procedure, and data processing methods used for the two-harvester study were applied to the larger array as well. The average power output and flutter frequency for each of the four harvesters when operating alone is given in Table 3.2.

Table 3.2 Comparison of the behavior of the four energy harvesters when operating alone with Re = 190,000.

Parameter	*Harvester 1*	*Harvester 2*	*Harvester 3*	*Harvester 4*
Steady State Power Output	1.50 mW	1.25 mW	1.54 mW	1.17 mW
Flutter LCO Frequency	4.80 Hz	4.88 Hz	4.89 Hz	4.91 Hz

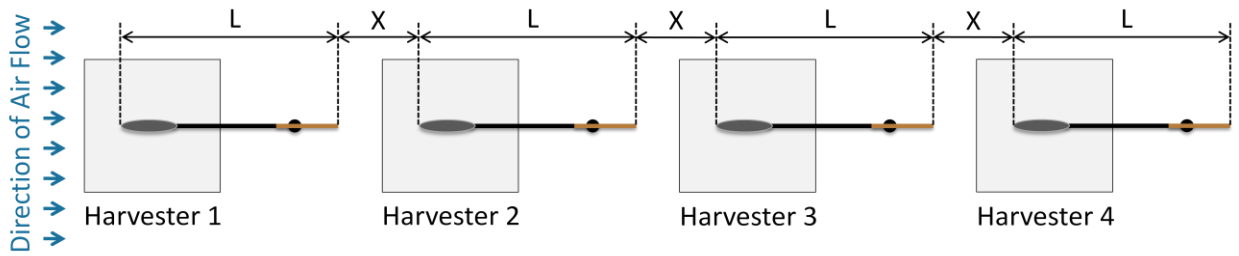

Figure 3.11 Overhead view of the four-harvester array with coordinates defined. All harvesters have the same overall length, L, and the same separation distance, X.

Experiments with the four harvester array revealed that the same frequency lock phenomena that occurred with two harvesters applied to the larger array. When operating simultaneously in the wind tunnel, all four harvesters fluttered at the same frequency for all the array spacings tested. Figure 3.12 plots the normalized power as a function of the harvester's position within the array, and Figure 3.13 plots the normalized power and array efficiency as functions of the separation distance. The results show that wake interaction effects continue to have significant influence on the power output of the array when the array is expanded to four harvesters. The normalized power output of the harvesters in the array varies with both the array

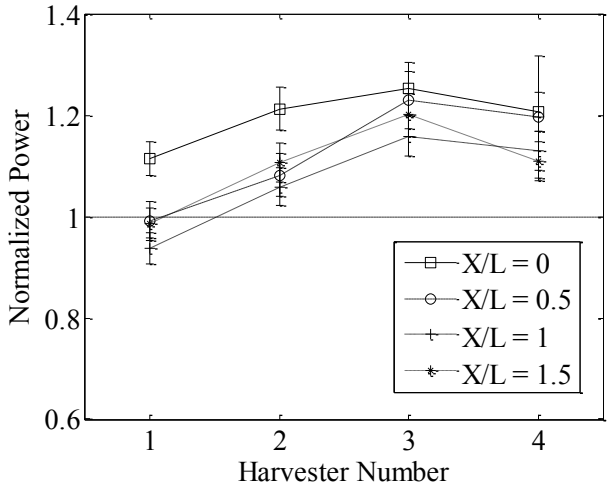

Figure 3.12 Comparison of the normalized power outputs of four flutter energy harvesters operating in an array with various stream-wise spacings. Harvester number increases from the leading harvester (number 1) to the trailing harvester (number 4). Error bars represent ± one standard deviation from the mean over 60 seconds of data.

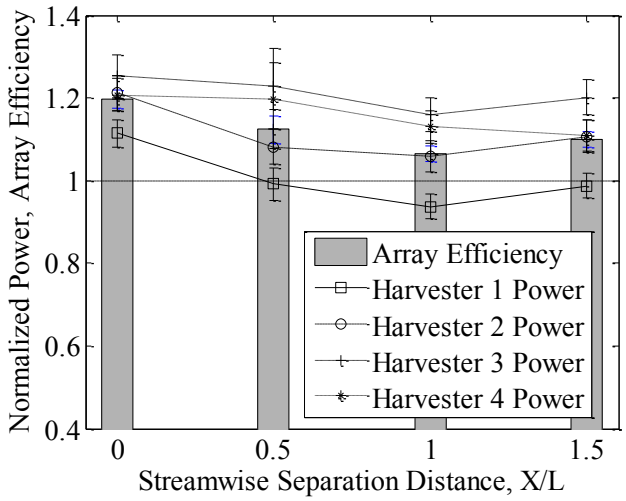

Figure 3.13 Normalized power output (lines) and array efficiency (bars) as functions of separation distance for the array for four flutter energy harvesters. Error bars represent ± one standard deviation from the mean over 60 seconds of data.

spacing and the harvester position within the array, with the third harvester in the group exhibiting the largest gain in power output regardless of the array spacing. The closest packed

configuration, X/L = 0, shows the largest benefit from the wake interactions, yielding the highest normalized power output for every harvester in the array. Notably, the X/L = 0 separation shows increased power output for not only the trailing devices, but also for the leading harvester in the array, while all other separations show that the leading harvester is largely unaffected by the presence of the downstream devices. This is consistent with the data for the two-harvester case as well, as shown in Figure 3.4. The four harvester array achieves array aerodynamic efficiencies greater than unity for all the separations tested, with a peak array efficiency of 120% occurring with zero separation distance.

5. Conclusions

This study has experimentally demonstrated that a series of passive aeroelastic energy harvesters arranged in tandem can achieve aerodynamic array efficiencies greater than 100%. This synergistic effect occurs due to an inverted drafting wake interaction phenomenon in which all the harvesters in the array phase lock in the same flapping frequency, and the downstream devices are excited to oscillate at larger amplitudes by the vortex wake. The frequency locking appears over a range of array spacings in spite of the fact that the individual devices flutter at slightly different frequencies when in isolation. For array configurations where the flutter frequencies differ, a beat phenomenon occurs, while for configurations where the flutter frequencies lock, the amplitudes of the voltage outputs are steady and the phase difference between the harvesters is linearly related to the separation distance, flutter frequency, and free stream wind speed. This simple relationship between the phase and array configuration would be important in designing circuits to amalgamate the power outputs of the energy harvesters.

In a two harvester array, we show that the beneficial inverted drafting exists when the trailing device is between 0 and 3 body lengths directly behind the leader and achieve a maximum aerodynamic array efficiency of 115% with a separation of two body lengths. Offsetting the trailing harvester in the cross-stream direction introduces an asymmetry in the system and breaks the frequency lock, with wake interaction effects effectively ceasing when the cross-stream separation is increased to one body length. When the array was expanded to four harvesters, the third harvester in the series exhibited the largest benefit due to wake interactions for all the array configurations tested. The aerodynamic array efficiency peaked at 120% with zero separation distance. Thus, the array configuration that is most spatially efficient is also the most aerodynamically efficient.

The synergistic wake interaction effect described here stands in contrast to the case for traditional rotary wind power devices. While further research will be necessary to optimize individual flutter energy harvesters for maximum efficiency and to ultimately determine if aeroelastic energy harvesting can be competitive with conventional turbine based devices, this study has demonstrated a novel and beneficial aerodynamic interaction effect that can be leveraged to enhance array performance. This ability of the flutter energy harvesters to extract additional energy from the vortex wake of an upstream device may be an inherent advantage of wind and water power devices based on passive flapping or oscillating structures rather than rotation.

REFERENCES

Alben, S., 2009, "Wake-Mediated Synchronization and Drafting in Coupled Flags," Journal of Fluid Mechanics, 641, pp. 489-496.

Beal, D. N., Hover, F. S., Triantafyllou, M. S., Liao, J. C., and Lauder, G. V., 2006, "Passive Propulsion in Vortex Wakes," Journal of Fluid Mechanics, 549, pp. 385-402.

Bose, N., and Lien, J., 1990, "Energy Absorption from Ocean Waves: A Free Ride for Cetaceans," Proc. R. Soc. Lond. B, 240, pp. 591-605.

Bryant, M. and Garcia, E., 2011, "Modeling and Testing of a Novel Aeroelastic Flutter Energy Harvester," Journal of Vibrations and Acoustics, 133**,** 011010.

Dowell, E. H., Curtiss, H. C., Jr., Scanlan, R. H., and Sisto, F., 1980, *A Modern Course in Aeroelasticity*, Sijthoff & Noordhoff, Alphen aan den Rijn, The Netherlands, Chap. 3.

Guyomar, D., Badel, A., Lefeuvre, E., and Richard, C., 2005, "Toward Energy Harvesting Using Active Materials and Conversion Improvement by Nonlinear Processing," IEEE Trans. on Ultrasonics, Ferroelectrics, and Frequency Control, 52(4), pp. 584-595.

Hau, E., 2006, *Wind Turbines: Fundementals, Technologies, Appications, Economics*, Springer, Berlin, Germany, Chap. 16.

Hodges, D. H., and Pierce, G. A., 2002, *Introduction to Structural Dynamics and Aeroelasticity*, Cambridge University Press, Cambridge, UK, Chap. 4.

Jain, P., 2011, *Wind Energy Engineering*, McGraw-Hill, New York, USA, Chap. 8.

Jia, L. B. and Yin, X. Z., 2008, "Passive Oscillations of Two Tandem Flexible Filaments in a Flowing Soap Film," Physical Review Letters, 100, 228104.

Kim, S., Huang, W. X., and Sung, H. J., 2010, "Constructive and Destructive Interaction Modes between two Tandem Flexible Flags in Viscous Flow," Journal of Fluid Mechanics, 661, pp. 511-521.

Liao, J. C., Beal, D. N., Lauder, G. V., Triantafyllou, M. S., 2003, "The Kármán Gait: Novel Body Kinematics of Rainbow Trout Swimming in a Vortex Street," J. Experimental Biology, 206, pp. 1059-1073.

Ristroph, L. and Zhang, J., 2008, "Anomalous Hydrodynamic Drafting of Interacting Flapping Flags," Physical Review Letters, 101, 194502.

Theodorsen, T., 1934, "General Theory of Aerodynamic Instability and the Mechanism of Flutter," NACA Report No. 496, pp. 413-433.

Yarusevych, S., Sullivan, P. E., Kawall, J. G., 2009, "Smoke-Wire Flow Visualization in Separated Flows at Relatively High Velocities," AIAA Journal, 47(6), pp. 1592-1595.

Zhu, L., 2009, "Interaction of Two Tandem Deformable Bodies in a Viscous Incompressible Flow," Journal of Fluid Mechanics, 635, pp. 455-475.

This chapter originally appeared as:

Bryant, M., Mahtani, R. L., and Garcia, E., 2012, "Wake Synergies Enhance Performance in Aeroelastic Vibration Energy Harvesting," Journal of Intelligent Material Systems and Structures, (In Review).